

# Role of metasomatism in the development of the East African Rift at the Northern Tanzanian Divergence: Insights from 3D magnetotelluric modelling.

Sinan Özaydın<sup>1</sup>, Kate Selway<sup>2,3</sup>, Stephen F. Foley<sup>4</sup>, Isra S. Ezad<sup>4</sup>, William L. Griffin<sup>4</sup>, Pascal S. Tarits<sup>5</sup>, Sophie Hautot<sup>6</sup>

<sup>1</sup>School of Geosciences, University of Sydney, Sydney, Australia

<sup>2</sup>School of Natural Sciences, University of Tasmania, Hobart, Australia

<sup>3</sup>Vox Geophysics, Perth, Australia

<sup>4</sup>School of Natural Sciences, Macquarie University, Sydney, Australia

<sup>5</sup>Laboratoire Géosciences Océan, Institut Universitaire Européen de la Mer, 29280 Plouzané, France

<sup>6</sup>IMAGIR sarl, 29290 Saint Renan, France

## Key Points:

- 3D magnetotelluric models of North Tanzanian Divergence are converted to water in mantle models to map metasomatism in the region.
- Melting events in the Mozambique Belt caused metasomes to be destroyed and the lithospheric mantle to be dehydrated.
- The rifting in the region might be limited if there is no supply of metasomatic material towards the rift zone.

## Abstract

The Northern Tanzanian Divergence in the East Africa Rift is arguably the best place on Earth to study the controls on rifting of thick lithosphere. Here, where the East Africa Rift intersects the Tanzanian Craton and the Mozambique Belt, the relationships between volcanism, faulting, pre-existing structures and lithospheric thickness and composition can be observed. In this work, we carry out the first lithospheric-scale 3D magnetotelluric modelling of the Northern Tanzanian Divergence and combine the results with experimental electrical conductivity and petrology models to calculate mantle composition, which is also inferred in the craton from reanalysis of garnet xenocryst data. Our results show that metasomatic materials exist in the cratonic lithospheric mantle and the relatively undeveloped southern part of the rift zone. However, the lithospheric mantle of the Mozambique Belt and the more developed northern section of the rift is more resistive and does not contain metasomatic phases. Combined with geochemical data from erupted lavas, these results suggest that, in zones that have experienced voluminous Cenozoic magmatism, melting events have destroyed the metasomes and dehydrated the mantle. Since the presence of magma is a primary control of lithospheric strength, rifting may become limited as the lithospheric mantle becomes dehydrated and harder to melt.

## Plain Language Summary

The motion of tectonic plates relies on a specific set of physical conditions. Continental breakup or rifting occurs when certain parts of the lithosphere are weak, and when stress applied to these regions is sufficient. Weaknesses in the lithosphere rely on its composition and pre-existing structures. We can image and analyse these features using the magnetotelluric method, a geophysical technique that maps electrical conductivity variations within the Earth. Our results show that compositionally weakening agents (metasomes) play an essential role in the development of the rift by making the mantle easier to melt. We also image some portions of the rift that do not contain such agents, suggesting that melts may have dried out these parts of the lithosphere, leaving a dry and resistive residue. This situation may indicate that melting in the region might be limited in the long run due to the absence of these materials.

## 1 Introduction

The initiation and evolution of intracontinental rifts are fundamental to the theory of plate tectonics. Most simply put, they begin to develop when the stresses applied can overcome the strength of the lithosphere. The intricate interplay between the distribution of stress, magmatism, pre-existing lithospheric architecture, mantle composition and rheology can result in a variety of rifting styles (Brune et al., 2023). The East African Rift System (EARS) is the largest active continental rift system in the world and displays various stages of rift development along its strike length (Boone et al., 2019). In this study, we focus on the region where the EARS meets the Tanzanian Craton at the North Tanzanian Divergence (NTD). Here, the rift structure widens and there is an increase in the geochemical variety and volume of volcanism. The geochemical characteristics of lavas and mantle xenoliths in the NTD reflect the evolving nature of the lithosphere through the Cenozoic in response to plate reorganisation and plume impingement (Foley et al., 2012; Rooney, 2020; Mana et al., 2015; Baptiste et al., 2015).

Magnetotellurics (MT) is a powerful tool to reveal the composition and architecture of the lithosphere-asthenosphere system (Naif et al., 2021; Selway, 2014; Selway & O'Donnell, 2019). It is especially sensitive to interconnected secondary conductive phases (e.g., melts, hydrous minerals) and water ( $OH^-$  bound to nominally anhydrous minerals), which are often products of metasomatism. Since deformation by diffusion creep in olivine is water-dependent (Hirth & Kohlstedt, 2003), these metasomatised and hydrated regions are more

likely to be rheologically weaker. The same regions are also often more prone to melting since they contain components such as  $H_2O$  or  $CO_2$ , which cause a substantial drop in the solidus temperature (Foley & Pintér, 2018), and metasomatic phases that are easier to melt, such as hydrous pyroxenites (Foley et al., 2022). Moreover, regions rich in metasomes are now envisaged as one of the reasons that such thick lithosphere can initiate rifting (Rooney, 2020; Foley & Fischer, 2017), where the metasomes provide a weaker lithosphere either through the existence of melt (Buck, 2006) or the combined effect of the hydrolytic weakening of olivine and/or grain size reduction (Selway, 2015).

It has been demonstrated that MT can be useful in understanding the relationship between mantle composition and magmatic processes. For instance, (Özaydın & Selway, 2022) used MT models to show that kimberlites might exploit the "lithospheric fuel" frozen in metasomatised mantle in order to ascend. However, the effects of large-volume magmatism (e.g., basalts) on the composition of the lithosphere need to be better understood (Özaydın et al., 2022), since they could possibly exhaust these metasomes and dehydrate the mantle as well. Consequences of such dynamics may be crucial for rift development (Muirhead et al., 2020; Foley & Fischer, 2017).

Previous research in the NTD has combined MT and seismic tomography studies to reveal the existence of melt within the crust of the rift zone, mainly around the Manyara fault (Plasman et al., 2019; Tiberi et al., 2019; Clutier et al., 2021; Reiss et al., 2022). 2D modelling of long-period MT data has also imaged the large-scale lithospheric structure in the area, with results suggesting that water content is higher in the cratonic lithosphere than the rift and is not therefore the primary control on deformation localization (Selway, 2015).

Here, we image the deep electrical structure in NTD with 3D MT modelling utilising the combined MT datasets of Selway (2015) and Plasman et al. (2019). Electrical conductivity variations in the mantle can be used to make quantified interpretations of composition employing experimental electrical conductivity and petrology studies (Özaydın & Selway, 2020; Selway, 2014). We made these calculations using the software MATE (Özaydın & Selway, 2020) and a geophysically-constrained thermal model (Afonso et al., 2022). In the cratonic domain, we also constructed lithological sections from the garnet xenocryst database (Griffin et al., 1991; O'Reilly & Griffin, 1996), using the methods described in Griffin et al. (2002). Using the MT model, we checked for the presence of water, melt, and other conductive phases. We compared these results with the current knowledge from geochronological studies, geochemical modelling, mantle xenoliths/xenocrysts and other geophysical studies to form a better understanding of the geodynamics of the region.

## 2 Geological Background

The rocks of north-eastern Tanzania record more than 2.5 billion years of continental evolution, including cratonisation, rifting, collision and multiple episodes of reactivation of lithospheric-scale structures. The Tanzania Craton amalgamated by c. 2.6 Ga (Chesley et al., 1999; Many et al., 2006; Thomas et al., 2016) and geophysical studies suggest that the lithosphere has seismic wavespeeds typical of cratonic domains to depths of at least 150 km (e.g., Afonso et al., 2022; Mulibo & Nyblade, 2013b; Emry et al., 2019; O'Donnell et al., 2013), with low surface heat flows (Nyblade, 1997). The cratonic lithosphere has been sampled by Jurassic to Quaternary kimberlite magmatism and Tertiary to Recent rift-related volcanism (e.g., Foley et al., 2012; Rooney, 2020). Petrographic and geochemical analyses of xenoliths show evidence that the cratonic lithosphere has been metasomatised during multiple events since the Archean (e.g., Koornneef et al., 2009; Stachel et al., 1998; Chesley et al., 1999; Baptiste et al., 2015; Aulbach et al., 2011). This agrees with MT models that show the cratonic lithosphere is likely to be hydrated and metasomatised (Selway, 2014, 2015).

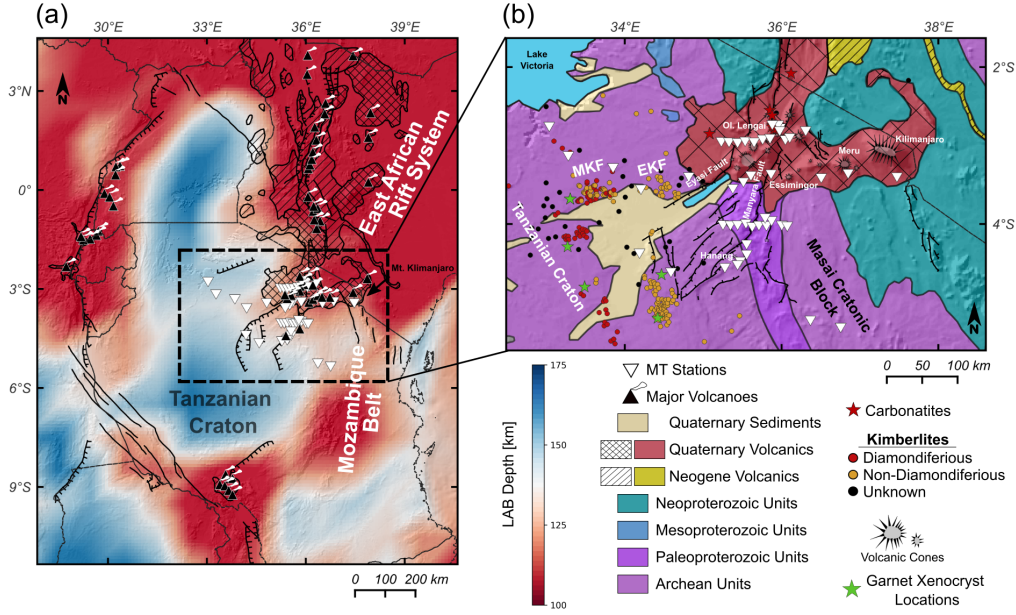


**Figure 1.** Maps showing the study area: (a) Main tectonic units, active volcanoes and Cenozoic volcanic units of Eastern African Rift System overlain on LAB depths derived from the study of Afonso et al. (2022). (b) Geological map of the main study area alongside MT stations, kimberlite locations (Giuliani & Pearson, 2019), and Cenozoic volcanic rocks derived from the GeoRoc database (Lehnert et al., 2000). MKF: Mwadui Kimberlite Field, EKF: Eyasi Kimberlite Field.

After cratonisation, the first major tectonic event to affect the north-east Tanzania Craton was the Neoproterozoic East African (or Pan-African) Orogen, which was associated with the amalgamation of East and West Gondwana and formed the Mozambique Belt as part of an extensive band of deformed lithosphere that extends from East Africa into Antarctica (e.g. Stern, 1994; Grantham et al., 2003). Despite the Neoproterozoic timing of deformation, isotopic and geochronological data from across the Mozambique Belt show that it consists largely of reworked Archean lithosphere, including protoliths with ages similar to Tanzanian Craton rocks (e.g., Maboko, 2000; Thomas et al., 2016), implying that the Tanzania Craton may have originally extended further to the east than its present extent. Peak East African Orogen metamorphism occurred at c. 640 Ma (Muhongo et al., 2001) and was followed by a period of relative quiescence.

North-eastern Tanzania is currently being deformed as part of the East African Rift (Ebinger, 2012), the most extensive and best exposed active continental rift on Earth, which extends from Ethiopia to Malawi. Seismic tomography models show relatively slow wavespeeds at lower to upper mantle depths beneath central and eastern Africa and a thinned mantle transition zone, which is interpreted to be caused by a hot mantle plume impinging on the base of the African lithosphere (e.g., Mulibo & Nyblade, 2013a; Emry et al., 2019; Hansen et al., 2012; O'Donnell et al., 2013; Ritsema et al., 1999). The geochemistry of Cenozoic magmas support the existence of a plume underlying East Africa, with evidence for elevated mantle temperatures and plume magma sources (Rooney et al., 2012; Rooney, 2020). The initial plume impact is interpreted to have occurred c. 30-40 Myr ago (Ebinger & Sleep, 1998; Hofmann et al., 1997). Geodynamic models suggest that the present rifting is dominantly caused by deviatoric stresses induced by plume-related uplift (Stamps et al., 2014; Koptev et al., 2016) and much of the deformation has reactivated pre-existing



structures, including those formed during the East African Orogen, suggesting that they have continued to be zones of lithospheric weakness (e.g., Daly et al., 1989; Tommasi & Vauchez, 2001).

The character of the East African Rift changes markedly along its extent, from incipient oceanic spreading in the northern part of the rift to the first gasps of magmatism in the Rungwe Province, south of the Tanzanian Craton. Where it meets the Tanzanian Craton, the rift bifurcates into Eastern and Western Branches, seemingly following weaker lithosphere that surrounds the strong craton. The NTD is the section of the Eastern Branch in north-eastern Tanzania and is characterised by a relatively broad zone of volcanism and block faulting (Tiberi et al., 2019; Le Gall et al., 2008; Clutier et al., 2021). The Eyasi and Manyara rifts extend into the eastern margin of the Tanzania Craton, and the volcanic centres at Labait and Hanang have sampled cratonic lithosphere that is being actively impacted by the plume (Le Gall et al., 2008), making this an ideal location to study the controls on continental rifting. As is the case for the broader rift, faulting and volcanism tend to follow pre-existing zones of weakness. Volcanism in the NTD initiated at c. 6 Ma at locations in the west of the NTD close to the edge of the craton; with time new volcanic centres have erupted further to the east, while volcanism has continued and spread in the west, including to Oldoinyo Lengai, the only active carbonatitic volcano on Earth (Mana et al., 2015). While the timing of faulting is harder to quantify, most faulting appears to have occurred in the last 4 Myr and movement on individual faults appears to be temporally correlated with volcanism (Le Gall et al., 2008).

### 3 Methods

#### 3.1 Magnetotelluric Data and Modelling

MT data used in this study are a compilation from stations published previously (Selway, 2015; Plasman et al., 2019). These data include the 21 long-period stations reported in Selway (2015), which were from a regional study around the North Tanzanian Divergence (green triangles, Figure 1b), and 24 broad-band stations from Plasman et al. (2019), from a study focused more on the rift zone (white triangles, Figure 1b). The long-period data also included tipper data, which was included in the inversion. Some of the stations are excluded from the broad-band dataset due to the limitations that arise from cell sizes constructed for the large-scale model. For this problem, we eliminated the most locally similar-looking stations to avoid loss of information in the long periods.

Three-dimensional magnetotelluric inversions were carried out using the ModEM algorithm (Kelbert et al., 2014). The 3D nature of the area is apparent both from the high phase tensor skew degrees observed at all frequency ranges and highly variable strike directions (Figure 3), which require three-dimensional MT modelling techniques to obtain reliable results (Booker, 2014). The horizontal discretization in the core region was chosen to be 5 km in both directions. Outside the core region, we inserted seven padding cells with widths that increase by a factor of 1.5. In the vertical domain, we used a total of 53 cells with depths that increase by a factor of 1.15, starting from the third cell with a thickness of 150 m. We choose to add three 50 m layer cells at the top of the model to partially mitigate the problems that may arise from galvanic distortion (Kelbert et al., 2014). The total depth in the vertical direction is  $\sim 705$  km. The ocean is dealt with by inserting fixed  $0.3 \Omega m$  valued cells according to global topography/bathymetry data ETOPO1 (Amante & Eakins, 2009).

We performed the inversion in two main stages. In the first stage, we inverted only the tippers from the long-period stations at 25 frequencies between 1 to 10000 s. The errors on the tipper were fixed at a single value of 0.05. The initial model was constructed as a homogeneous half-space with  $210 \Omega m$  resistivity, which is the median determinant apparent resistivity value calculated from impedance tensors from all stations between 100 to 10000 s. An isotropic covariance matrix was constructed using the value of 0.5 in all directions.

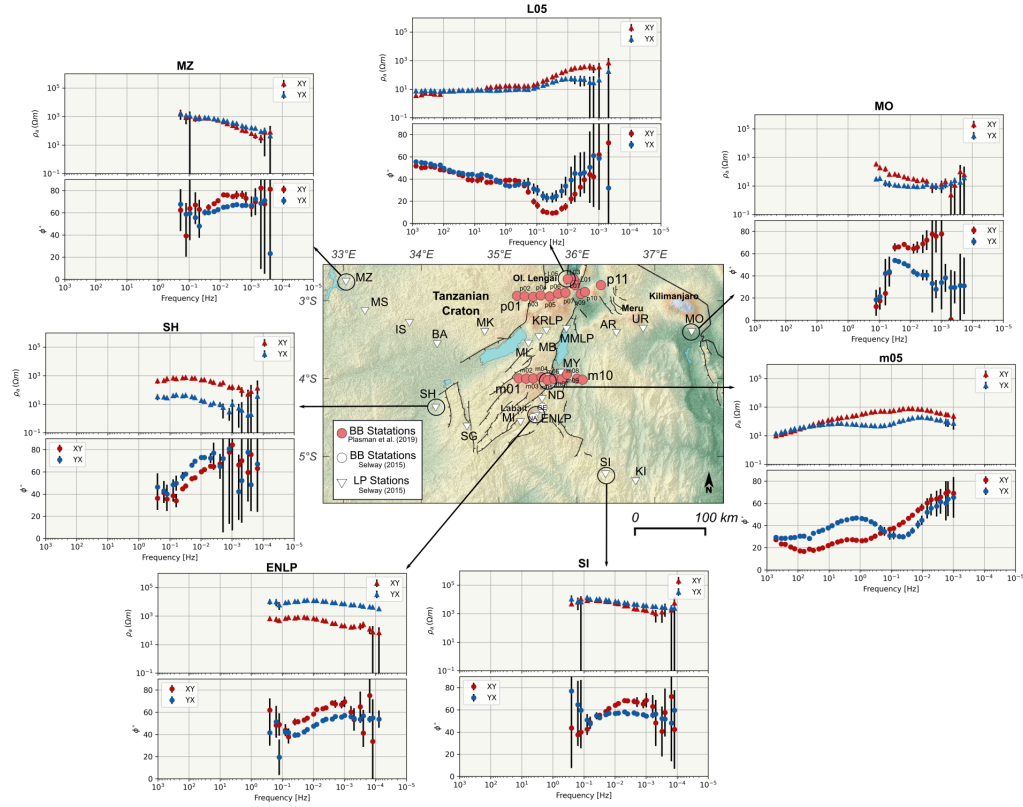


**Figure 2.** Apparent resistivity and phase curves of selected off-diagonal stations used in the inversions. More information on data can be found in Figures S7-52. LP: Long Period, BB: Broad-band.

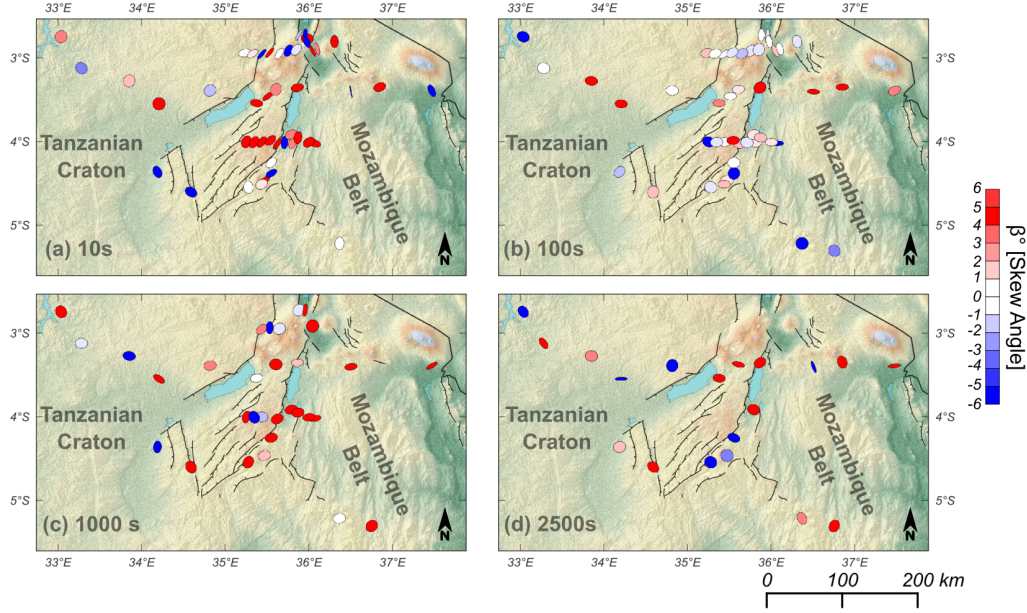


**Figure 3.** Phase tensor ellipses filled with skew angles ( $\beta^\circ$ ) for (a) 10, (b) 100, (c) 1000, and (d) 2500 seconds. Absolute skew angles above the value of  $3^\circ$  are considered to be out of the practical limits of reliable 2D MT modelling (Booker, 2014).

The initial regularization parameter ( $\lambda$ ) was selected as 10 and set to decrease by a factor of 5 when the RMS difference between subsequent iterations became less than 0.002. The inversion ran for 55 iterations until it converged to a final RMS value of 1.59, starting from 3.48.

In the second stage of inversion, we inverted both the full impedance tensor and tipper data, using the result from the tipper inversion as the initial model. The error floors were chosen to be 5 % of  $\sqrt{Z_{xy}Z_{yx}}$  for all impedance tensor elements. We chose to decrease the constraints on tipper data with an error of 0.15 to give more weight to impedances in this stage of the inversion. Twenty-five frequencies between 1 and 10000 s were inverted. The inversion was conducted with the same regularization parameter and reduction scheme as the first stage of the inversion, and the isotropic covariance value was reduced to 0.3. We also ran the inversions with covariance values and observed no crucial differences that would affect our interpretations (Figure S2-3). Inversion started with an initial RMS value of 16.25 and finalized with a value of 2.52. The local RMS values can be seen in the RMS map of impedance fittings (Figure S6) and individual graphs (Figures S53-115).

Sensitivity tests on the resistivity models were performed on the conductors  $C_1$  and  $C_M$  to test their robustness. We masked these conductive regions with blocks in electrical resistivities varying between  $1 \Omega m$  and  $10000 \Omega m$  (Figures S4-5). The results demonstrated that both conductors appear robust and applicable for interpretation in the models.

### 3.2 Water content calculations and compositional solutions to electrical conductivity

The electrical conductivity distribution of the mantle can be used to calculate mantle water content with the aid of experimental electrical conductivity measurements, a water-distribution model between phases and a temperature model (Özaydın & Selway, 2020). By

“water” here, we refer to the  $OH^-$  within melts, hydrous minerals and nominally anhydrous minerals (NAMs) such as olivine and pyroxenes. There can be multiple compositional causes for anomalously electrically conductive regions in the mantle (Özaydın et al., 2021), such as the existence of hydrous phases (e.g., phlogopite, amphibole), melts, and other minor accessory minerals (e.g., magnetite, graphites and sulphides, Ten Grotenhuis et al., 2005; Dai et al., 2019). Since this “water” is a general product of mantle processes that modify the composition of the mantle and almost exclusively exist along with other metasomatic phases (e.g., Peslier et al., 2012), we use it as a general proxy for mantle metasomatism in the maps and sections in the figures in this study. Along the A-A’ transect, we also specifically calculated phlogopite contents in a dry lherzolitic matrix 10 km below the LAB (Figure 6e). For all compositional calculations, the MATE software was used (Özaydın & Selway, 2020).

Experimental electrical conductivity studies in mantle phases carried out during the last two decades have shown that conductivity in most mantle minerals is controlled by semi-conduction mechanisms with varying degrees of temperature dependence ( $T$ ), which can be defined with an Arrhenian formalism (Equation 1; Özaydın & Selway, 2020; Dai et al., 2020).

$$\sigma = \sigma_0 \exp\left(-\frac{\Delta H}{RT}\right) \quad (1)$$

where  $\sigma_0$  is pre-exponent (S/m),  $\Delta H$  is the activation enthalpy, and  $R$  is the gas constant. For the NAMs, the electrical conduction processes can be described as a summation of three conduction mechanisms that operate on different temperature levels: ionic ( $\sigma_{ion}$ ), polaron ( $\sigma_{ion}$ ) and proton ( $\sigma_{pro}$ ) conduction (Equation 2).

$$\sigma = \sigma_{ion} + \sigma_{pol} + \sigma_{pro} \quad (2)$$

For the depths in which we are interested in this study, polaron and proton conduction are the most relevant conduction mechanisms, and relate to the electrical conductivity of dry and hydrated minerals, respectively. While electrical conductivities of silicate minerals have high temperature dependencies (high activation enthalpy), there are some other phases such as graphite and sulphides that have very low temperature dependencies (low activation enthalpy; Özaydın & Selway, 2020).

The model for water distribution among NAMs is constructed using the water partitioning coefficients shown in Table 1. We sought solutions of water contents between a dry lithosphere and bulk water solubility values calculated using water partitioning coefficients, based upon the sub-solidus olivine water solubility model of Padrón-Navarta & Hermann (2017). Since this model limits water solubility to low levels (several tens of ppm) in the shallow lithospheric mantle, we cannot use water content as a proxy for metasomatism in most of the uppermost lithosphere ( $< 70 - 90$  km). Therefore, one has to be mindful while interpreting our figures in terms of how metasomatism translates to different signatures going from the lower lithosphere ( $> 70 - 90$  km) to above. One can most easily do this by looking at resistivity and water content maps in tandem and checking whether a conductor originates from water-rich/metasomatised areas.

We have used the electrical conductivity models of Gardés et al. (2014), Dai & Karato (2009a), Liu et al. (2019), and Dai & Karato (2009b) for olivine, orthopyroxene, clinopyroxene and garnet, respectively. For the conductivity of phlogopite, the model of Li et al. (2017) was utilised with a fluorine content of 0.52 w.t. % (average fluorine content value in mantle rocks, Özaydın et al., 2022). All electrical conductivity models are corrected for the water measurement calibrations of Withers et al. (2012) for olivine, and Bell et al. (1995) for pyroxenes and garnet if needed. A lherzolitic composition was used to calculate the water contents in the region (Table S1). The use of different mantle peridotitic modal compositions

**Table 1.** Mineral water partitioning coefficients used in this study.

	Water Partitioning Coefficient	Reference
Orthopyroxene/Olivine	$D_{opx/ol} = 5.6$	Demouchy et al. (2017)
Clinopyroxene/Olivine	$D_{cpx/ol} = D_{opx/ol} \times 1.9$	Demouchy et al. (2017)
Garnet/Olivine	$D_{gt/ol} = 0.8$	Novella et al. (2014)

has been shown to have a negligible effect on understanding the variations of metasomatism (Özaydın & Selway, 2022). The Generalised Archie’s Law (Glover, 2010) was used for phase mixing to calculate bulk electrical conductivity. Interconnections for the minerals are constructed with cementation components of  $m = 2$  for orthopyroxene,  $m = 4$  for clinopyroxene and garnet and  $m < 1$  for olivine, which gives results close to Hashin-Shtrikman lower-bound (Özaydın & Selway, 2020). The thermal model used in these calculations is taken from multi-observable probabilistic inversions of Afonso et al. (2022).

Water measurements made on xenoliths from Labait, Lashaine, Olmani and Pello Hill were also compared with the MT-derived water models (Baptiste et al., 2015; Hui et al., 2015). To compare the bulk water contents, we used only the water measurements made on orthopyroxenes since they represent a more reliable water recorder than olivine (Yang et al., 2019). We converted orthopyroxene water contents to bulk water contents assuming the same partition coefficients used in MT-derived water models and composition. We have also used individual sample-based modal compositions in this conversion, which are indicated with different symbols (Figure 6). The orthopyroxene water contents reported in Baptiste et al. (2015) were measured with calibration of Paterson (1982), which is known to underestimate the water contents (Demouchy & Bolfan-Casanova, 2016). We corrected these values by multiplying the water contents by 3 (Demouchy & Bolfan-Casanova, 2016).

### 3.3 Garnet xenocryst analyses

The data used for this analysis includes the garnet xenocrysts previously used in studies with older methods (Griffin et al., 1991; O’Reilly & Griffin, 1996). Garnet (pyrope) xenocrysts derived from kimberlites can be analysed to understand the compositional structure of the underlying lithosphere, with the aid of thermobarometry (Ryan et al., 1996) and geochemical classification schemes (Griffin et al., 2002; Grütter et al., 2004). We analysed 276 garnet xenocrysts derived from five kimberlite pipes on the Tanzanian Craton (Green stars, Figure 1). We constructed a  $36 \text{ mWm}^{-2}$  generalised continental paleogeotherm to the  $P_{Cr}^{max} - T_{Ni}$  equilibrium conditions (Figure 4 Hasterok & Chapman, 2011). This geotherm is kinked parallel to the diamond-graphite transition at the temperature (950 °C) corresponding to the base of the depleted lithosphere (160 km), following the commonly observed distribution of  $P_{Cr}^{max} - T_{Ni}$  parallel to this trend (Griffin et al., 2003). The temperature at the base of the depleted lithosphere is determined by the sharp decrease in the population of garnets with Yttrium values less than 10 ppm (Figure S1). In order to determine the depth of origin of the garnet grains and construct the compositional sections, calculated garnet equilibrium temperatures were projected onto the defined paleogeotherm.

The constructed geotherm, alongside garnet major- and trace-element compositions, can be used to make compositional sections of the lithosphere. We use two garnet xenocryst classification schemes to understand the nature of the lithosphere. The first one is the CARP method (Cluster Analysis by Regressive Partitioning; Griffin et al., 2002), which shows the proportion of garnets derived from five different lithologies: (1) Depleted harzburgites, (2) Depleted lherzolites, (3) Depleted lherzolites with phlogopite metasomatism, (4) Fertile lherzolites, and (5) Melt-metasomatised lithologies. The other classification scheme (Figure Xc,d), taken from the work of Grütter et al. (2004), determines whether the host lithology



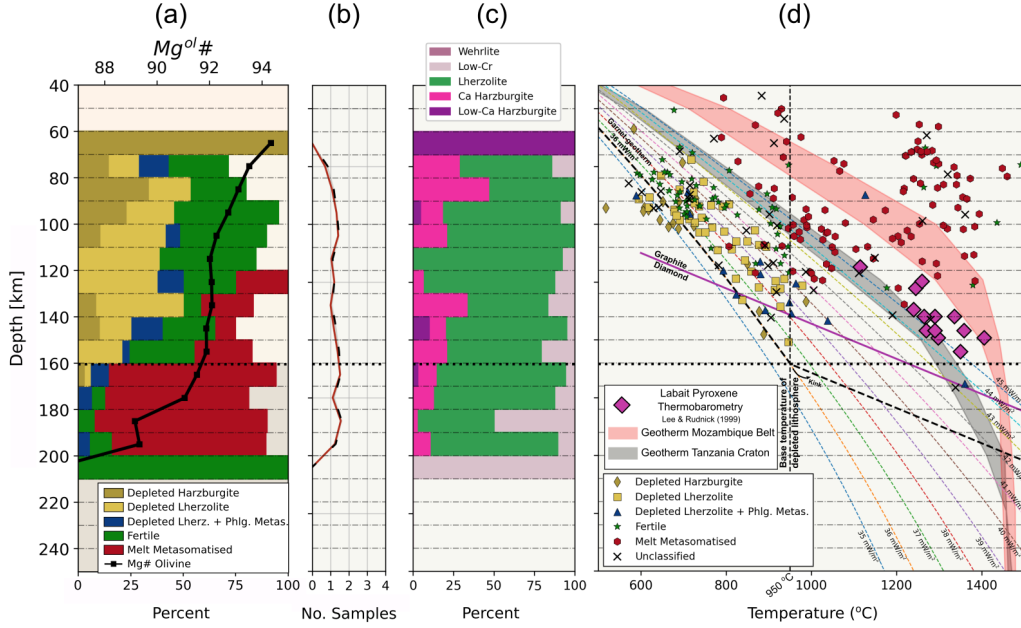


**Figure 4.** Mantle composition sections derived from kimberlite-derived garnet xenocrysts on the Tanzanian Craton (Green stars, Figure 1), alongside geophysical and xenolith-based geotherms. (a) CARP mantle composition section using the methodology of Griffin et al. (2002). (b) The number of samples analysed in with CARP methodology. (c)  $CaO - Cr_2O_3$  based mantle section based on the classification scheme of Grütter et al. (2004). (d) Geotherms constructed with garnet-xenocrysts alongside geotherms extracted from the geophysical thermal model of Afonso et al. (2022), for the Tanzanian Craton (grey) and Mozambique Belt (red). The pink diamond markers indicate the pyroxene-based thermobarometric calculations derived from xenoliths from Quaternary lavas in Labait (Lee & Rudnick, 1999). The black dashed line indicates the base of the depleted lithosphere.

is harzburgite, lherzolite, wehrlite, megacrystic, Ti-metasomatised, pyroxenite or eclogite based on garnet  $CaO - Cr_2O_3$  contents. Thermobarometry and classifications were made using the python library Thermobar (Wieser et al., 2022), specifically using the Cr-pyroxene garnet thermobarometry method of Ryan et al. (1996).

#### 4 Electrical structure, metasomatism and volcanism in northern Tanzania

MT resistivity (reciprocal conductivity) models produced in this work are presented alongside water content calculations derived from the MT models and other relevant geological information (Figures 5-7). Horizontal depth slices of electrical resistivity at different lithospheric depths and water content calculations in the mantle are shown in Figure 5. The first two electrical resistivity slices, down to 25 km, include information from earthquake epicentres in the region, while the deeper slices include information on the distribution of solidified magmatic products. We also show vertical slices from the electrical resistivity model where MT stations are denser and form a profile (Figures 6,7).



#### 4.1 Cratonic domain

The first slice (A-A'), which is shown in Figure 6, traverses through the Tanzanian Craton, Mwadui kimberlite field (MKF, Figure 1), Cenozoic volcanics in the Rift Basin and the Mozambique Belt. A two-dimensional model of this same slice that uses only the long-period data along this transect was previously analysed in Selway (2015). In the westernmost (cratonic) side of A-A', we observe a prominent shallow mantle (50 - 100 km) conductor  $C_1$ . While the horizontal limits are the same, the depth of this conductor is shifted vertically upwards ( $\sim 50$  km) compared to the 2D model of Selway (2015). This change in conductor location might be due to the different regularization approaches of different inversion codes, the inclusion of more data points in the 3D inversion, and the more accurate modelling of 3D features. The nature of this conductor can be best explained by the deposition of temperature independent conductive materials such as graphite and sulphides via infiltrating metasomatic fluids. Such prominent lithosphere-spanning conductors within cratons have also been observed worldwide, such as the Curnamona Province in South Australia (Robertson et al., 2016) and the Bushveld Complex in Southern Africa (Özaydin et al., 2022).  $C_1$  is proximal to several large orogenic gold deposits, including Nyankanga (Sanislav et al., 2015) and Bulyanhulu, which are associated with mafic rocks and sulphides. Orogenic gold deposits elsewhere are underlain by prominent mid-lower crustal conductors (Kirkby et al., 2022) that have been interpreted to be related to sulphide- and carbon-rich fluids involved in the gold mineralisation. There is no low-velocity anomaly in the vicinity of  $C_1$  in the large-scale study of O'Donnell et al. (2013), indicating that either the conductor is caused by a feature with no strong seismic response (i.e., it is not caused by hydrous minerals), or that the resolution of the seismic model is too coarse to image any low velocities. We suggest that  $C_1$  is likely caused by interconnected minor conductive phases such as sulphides or graphite, and that with further investigation it may be related to the orogenic gold mineralisation.

Along the A-A' transect, we observe a good correlation with our calculated water content variations, the LAB depths acquired from the study of Afonso et al. (2022) and the base of the depleted lithosphere from garnet xenocrysts (Figure 4). Water content calculations demonstrate that the cratonic lithospheric mantle beneath this region is variably metasomatised (e.g., near  $C_1$ ). We calculate a maximum bulk water content approaching 750 ppm beneath  $C_1$ . Since hydrous minerals can also enhance mantle conductivity, we also considered combinations of phlogopite and water in NAMs that could explain the conductivity structures along this transect. To do this, we first added phlogopite with different degrees of interconnectivity to a dry lherzolite matrix and compared the resulting conductivities with those observed at 10 km above the LAB of Afonso et al. (2022) (Figure 6e). If the phlogopite grains are very well connected (Archie's Law  $m = 1.1$ ) very low volume percentages throughout the transect can match the observed conductivities ( $< 0.5$  %). On the other hand, non-connected phlogopites ( $m = 5$ ) require unrealistically large volumetric abundances to explain the conductivities (15 %). We calculated the effect of 15 % phlogopite in a lherzolite matrix on seismic velocities with the toolbox of Abers & Hacker (2016): this showed that such high phlogopite contents would result in a  $V_S$  of  $\sim 4.17$  km/s beneath  $C_1$  at 140 km depth, which is much lower than what was observed ( $\sim 4.5 - 4.6$  km/s, O'Donnell et al., 2013). The results, overall, suggest that amounts of phlogopite that fit the electrical conductivity values and the seismic model can only be present if they are moderately interconnected ( $m = 2.5$ ).

#### 4.2 Kimberlites on the Craton

Kimberlites that are coincident with our MT transect on Tanzanian Craton are situated in the Mwadui kimberlite field (MKF on Figure 1, 42% diamondiferous) and the completely barren Eyasi kimberlite field (previously unnamed, EKF on Figure 1, Giuliani & Pearson, 2019). The mantle composition section constructed from kimberlite-derived garnet xenocrysts displays a semi-depleted and metasomatised lithosphere above the base of the

depleted lithosphere at 160 km (Figure 4). Below this depth, melt-metasomatised low-Mg# garnets start to strongly dominate the population. Fe-rich, heavily metasomatised mantle has also reported from studies of diamond mineral inclusions from the Mwadui kimberlites (Stachel et al., 1998). The small diamond window between the diamond-graphite transition and heavily metasomatised area might explain the relatively low proportion of diamondiferous kimberlites in the area compared to southern African counterparts (O'Reilly & Griffin, 1996).

Compared to  $C_1$ , the uppermost mantle (Moho to 100 km depth) is more resistive but still damp (50-500  $H_2O$  wt ppm) in the region further east where the Mwadui and western Eyasi kimberlites erupted (Figure 6a). The distribution of kimberlites along the profile matches well with the previously described relationship of electrical conductivity/water content variations of the mantle and kimberlites worldwide (Özaydın & Selway, 2022), in which kimberlites tend to be emplaced through metasomatised lithosphere but also avoid the most electrically conductive/heavily metasomatised regions such as the region around the lithosphere-spanning conductor  $C_1$ .

### 4.3 Rift Basin and Cenozoic Volcanics

The types of Cenozoic volcanism in the  $\sim 250$  km wide band from Ngorongoro to Mt. Kilimanjaro are starkly different from the kimberlite magmatism within the Tanzanian Craton and its margins (Mana et al., 2015; Foley et al., 2012; Rooney, 2020). The products of volcanism also vary temporally and spatially within the rift zone, indicating that the underlying mantle source region has continually evolved in structure and composition over time (Rooney, 2020; Foley et al., 2012; Baudouin & Parat, 2020; Baudouin et al., 2016; Mattsson et al., 2013). It has been suggested that melting of lithospheric or sub-lithospheric peridotite might not be enough to explain the chemical variety of alkaline volcanic rocks in the region and a mixture of sources might be needed (Mana et al., 2015; Rooney, 2020; Foley et al., 2012). Non-peridotitic sources include ultramafic rock assemblages such as hydrous pyroxenites and, in cratonic lithosphere regions, MARID (Mica-Amphibole-Rutile-Ilmenite-Diopside) or PIC (Phlogopite-Ilmenite-Clinopyroxene) (Grégoire et al., 2002). It is not certain whether such rock assemblages would have an effect on the electrical conductivity of the mantle since they may not be connected over large distances, but they may still be susceptible to melting if a thermal anomaly is present at depths shallower than 150 km (Foley et al., 2012, 2022). At the same time, melting and magma migration events may have induced the dehydration, hydration or destruction of conductive metasomes in their source region, which could be picked up by the MT models. The parental magma sourced from these regions can also deposit conductive minerals along their ascent pathway, forming electrically conductive features elongated towards the crust (e.g., Özaydın et al., 2022; Heinson et al., 2018). A system of coated channels formed in this way could help to preserve minerals not stable in peridotites (Foley, 1992). Previous profile-based 3D MT models of the region showed possible magma channels at crustal depths correlating well with the main rift segments (Plasman et al., 2019), providing support for the control of magmatism via inherited structures in the region (Le Gall et al., 2008; Muirhead & Kattenhorn, 2018).

Unveiling the nature of magma/fluid infiltration at the trans-lithospheric scale may help us elucidate the processes related to magma generation, how magmas travel to the surface and what kind of compositional effects magmatic events have on the lithosphere. In our models, the rift zone is electrically heterogeneous (Figure 5), as has been observed in previous MT models of the East African Rift (Hübert et al., 2018; Meju & Sakkas, 2007; Dambly et al., 2023). This may reflect magmas and fluids exploiting pre-existing, lithosphere-scale weakness zones (Acocella, 2014; Muirhead & Kattenhorn, 2018). More precisely, we image lithospheric-scale conductors proximal to the Eyasi, Manyara and Natron rift fault systems. For instance,  $C_{M-2}$  and  $C_{M-3}$  may represent magma ascent pathways associated with the Manyara rift fault systems. Within the rift zone, all these ascent pathways are sourced from

a deeper, widespread, conductive/wet zone in the lithosphere, which we call  $C_M$  (Figures 5 - 6). This deep mantle conductor correlates with low seismic velocities in many different tomography studies (Clutier et al., 2021; Tiberi et al., 2019; Plasman et al., 2019). In larger scale seismic tomography studies, however, the low velocity zone consistently extends towards the northern Natron rift system and connects to Kenya rift (e.g., O'Donnell et al., 2013; Clutier et al., 2021; Mulibo & Nyblade, 2013b).

The conductor  $C_2$  sits under the Northern Crater Highlands where volcanoes Oldoinyo Lengai, Embagai, Loolmasin and Olmati are situated, while  $C_3$  sits under the volcanoes Essimigor, Tarosero and Monduli. These crustal conductors may represent the presence of active magma or the effects of past magmatism in the form of crystalline conductive material. The metasomatised portion of the deeper lithospheric mantle ( $C_M$ ) would then represent a plausible place for incipient melts to form in response to an oxidised ( $CO_2 + H_2O$ ) solidus (Pintér et al., 2021) since our calculations fitting electrical conductivities with water-induced melting do not reduce the solidus enough to meet the local geotherm and induce melting (Figure 8). Another possibility could be that magmas form by the melting of hydrous pyroxenites in the region, which matches with the geotherm at  $C_M$  at these depths (Figure 8, Foley et al., 2022). Following this, we can suggest that these melts originated around  $C_M$  in response to a sub-lithospheric heat source and may have used oblique lithospheric weakness zones represented by  $C_{M-2}$  and  $C_{M-3}$  to ascend, forming conductors by mineralising conductive phases along the way.

Alternatively, we can assume that the magmas do not necessarily travel along these oblique lithospheric zones of weakness and are instead emplaced vertically upwards from their source regions. This would be likely to happen if the lithosphere beneath the volcanoes is also metasomatised/hydrated to account for metasome-induced incipient melting. While we observe hydrated zones beneath most of the volcanoes in the region, the lithosphere beneath the Northern Crater Highlands, where Oldoinyo Lengai, Embagan and Kerimasi are situated, as well as the lithosphere underlying Mt Meru and Mt Kilimanjaro, appears less hydrous (Figures 5 - 7). One potential pattern, which would require more extensive MT coverage for confirmation, is that dehydrated mantle appears to coincide with the more recent volcanism, while more hydrated mantle coincides with dormant volcanism in the southwest of the model region (Figure 6 - 7, Mana et al., 2015). In this model, recent melt generation would have increased the resistivity of these regions by melting metasomatic phases and partitioning water into the melt (e.g., Novella et al., 2014) and melts would have migrated without precipitating any conductive phases. If this were to be true, we can envisage that the lithospheric pathways may be likely to be more conductive if they use a pre-existing weakness zone such as  $C_{M-2}$  and  $C_{M-3}$ , occupying a plate boundary (Manyara Fault). In either case, it is possible that narrow conductive zones caused by magma/fluid infiltration may exist but are too small to be resolved by the current coarse MT data coverage (Kirkby & Doublier, 2022). This might be especially true for magmatism in Mt Kilimanjaro and Mt Meru since they occur above relatively dry mantle without any visible conductive pathway connecting them to a metasomatised lithospheric source. Since our data are only collected in profiles, it is particularly hard to distinguish if melt migration pathways exist away from the MT sites where they are absent.

Mana et al. (2015) performed geochemical melt modelling and radiometric dating on the lavas from the region spanning the Crater Highlands in the west to Mt Kilimanjaro in the east and proposed a melt generation model involving four stages of magmatism. In this model, different parts of the lithosphere with veined metasomes are melted within a somewhat depleted lithosphere where they might have intermingled with sub-lithospheric peridotitic melt. We indeed observe that the roughly outlined areas related to the four stages (Figure 6) coincide with the dryer mantle as calculated from the MT model. From the geochemical and isotopic data, (Mana et al., 2015) propose that during Stage 1 and Stage 4, melting occurred at c. 110-140 km depth and involved melting of amphibole-rich veins, while Stage 2 and Stage 3 melting occurred at slightly shallower depths (c. 85-110

km), involved more decompression melting and that the contribution from hydrous veins was negligible. This pattern is consistent with an interpretation of the MT model whereby melting of metasomatic phases increases lithospheric resistivity. The lithospheric mantle beneath Stage 1 and Stage 4 volcanoes is resistive and dehydrated at depths greater than 110 km, consistent with the melting and destruction of any hydrous veins. In contrast, the lithospheric mantle beneath Stage 3 volcanoes and some Stage 2 volcanoes is still conductive and hydrated in the depth range 85–110 km from which melts were sourced, consistent with the geochemical data that hydrous veins did not melt to produce the erupted lavas.

Dehydration and destruction of metasomes since the eruption of the xenoliths also might explain the mismatch between the bulk xenolith water contents (Baptiste et al., 2015) and our MT-derived water models (completely dry instead of  $\sim 122 - 186$   $H_2O$  wt ppm from the Lashaine sample LS11, Figure 6). A similar mismatch between xenolith water contents and MT-derived water contents is also observed in samples from Eledoi and Pello Hill (Figure 7 Baptiste et al., 2015). Carbonatite metasomatism in the mantle is indicated by the chemistry of Lashaine and Olmani xenoliths, the famous carbonatite magmatism of Oldoinyo Lengai, measured  $CO_2$  fluxes from Manyara Basin (Muirhead et al., 2020), and the occurrence of wehrlite xenoliths (Aulbach et al., 2020). This suggests that the recent metasomatic events might not introduce hydration since the increased  $CO_2$  fugacity will lower the  $H_2O$  fugacity in the environment, lowering the hydration of NAMs in the region (Baptiste et al., 2015).

In the NTD, another set of water content measurements made on mantle xenoliths is available from the Labait volcano (Figure 7 Hui et al., 2015). Similar to the other regions for which xenolith water contents are known, the mismatch between the MT-derived and xenolith water contents is high in Labait. This mismatch is too high to be caused by specific water partition coefficients between NAMs. Even though there are some good matches between xenolith water contents with MT models (Özaydin et al., 2021), the universality of this correlation is not well studied. In several studies it has been suggested that NAMs from xenoliths emplaced at the surface might not accurately record the hydration state of the mantle since water may diffuse into the host magma during xenolith ascent (Denis et al., 2018; Wang et al., 2021; Demouchy & Alard, 2021). Another possible reason might be that other phases control the bulk electrical conductivity rather than water in NAMs. For instance, the observed conductivity might be due to interconnected phlogopite-rich regions reported in the Labait and Kwaraha xenoliths (Baudouin & Parat, 2020) or melts as suggested by seismic tomography studies (Clutier et al., 2021; Tiberi et al., 2019; Plasman et al., 2019). The volcanism here might represent the relatively undeveloped version of the rift in the Northern Crater Highlands and volcanism outside the rift-axis, where metasomes have not yet been destroyed and may induce melting in the region as for the younger ages of the lavas of Labait, Hanang and Kwaraha (Mana et al., 2015).

#### 4.4 Implications for the stability of the Tanzanian Craton and Rift Propagation

Tectonically, one of the most striking features about northeast Tanzania is the vastly different responses to stress between the Tanzanian Craton and the adjacent lithosphere in the Mozambique Belt and Rift Basin. The Mozambique Belt underwent deformation of the whole lithosphere during the Pan-African Orogeny and is currently being deformed again during rifting. In contrast, the Tanzanian Craton, or at least the surviving portion of the Tanzanian Craton (Ebinger et al., 1997), has remained relatively tectonically stable during these events, seemingly able to withstand stresses that elsewhere are enough to produce continental-scale deformation. The apparent strength of the Tanzanian Craton is highlighted by the fact that the East Africa Rift, after extending approximately linearly from the Main Ethiopian Rift to the northern margin of the Tanzanian Craton, then bifurcates around the Tanzanian Craton and splits into the Eastern Branch, which we image here, and the Western Branch (Fig. 1). This contrasting behaviour indicates that there are significant rheological differences between the Tanzanian Craton and the adjacent lithosphere.



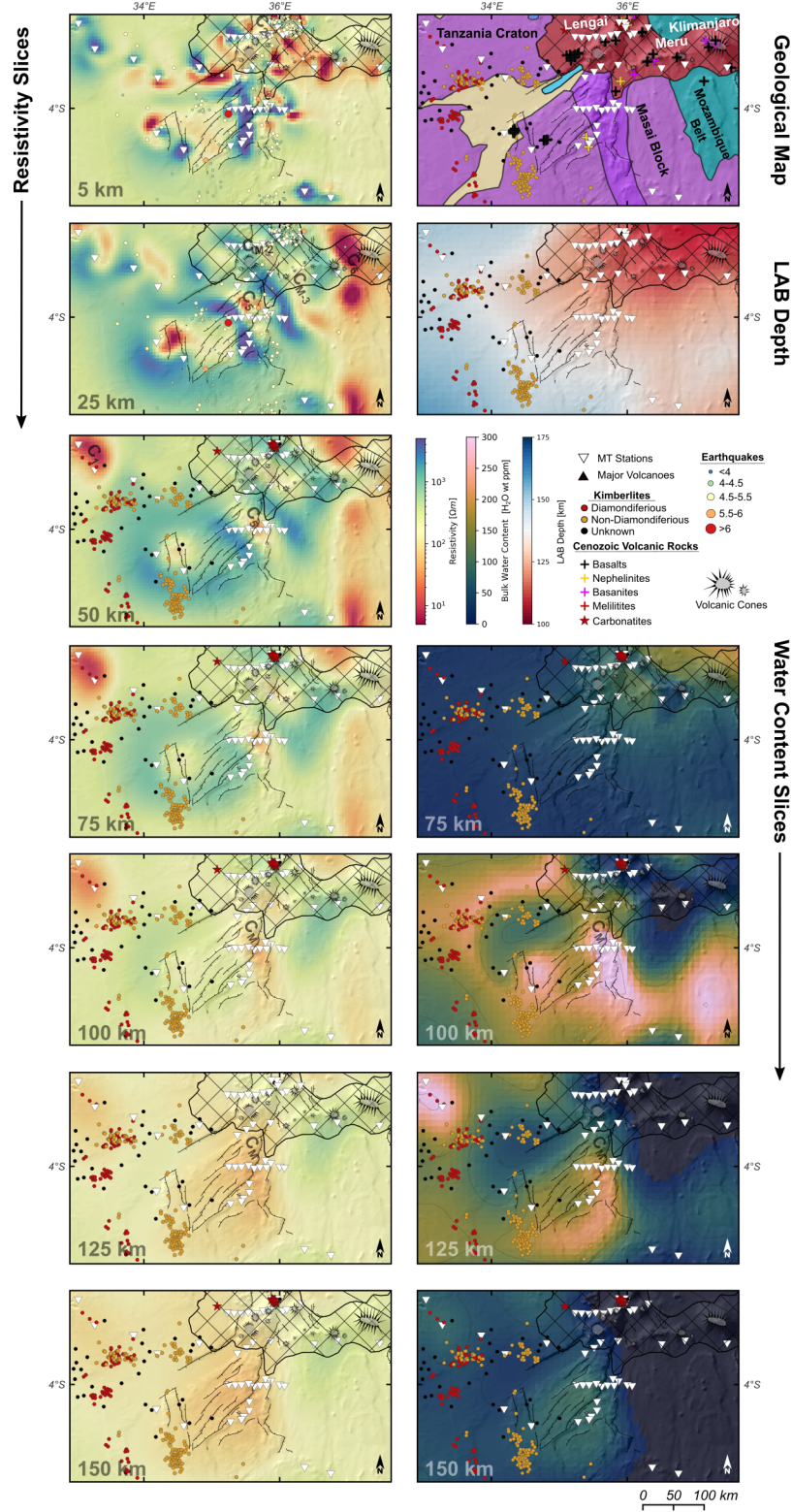


**Figure 5.** Horizontal electrical resistivity slices alongside water content calculations. The first map includes information on earthquake epicentres taken from USGS EarthExplorer. Slices deeper than 50 km include the location of kimberlites (Giuliani & Pearson, 2019) and Cenozoic volcanic rocks found in the GeoRoc geochemical data repository (Lehnert et al., 2000). More information on the geological map can be seen in Figure 1.

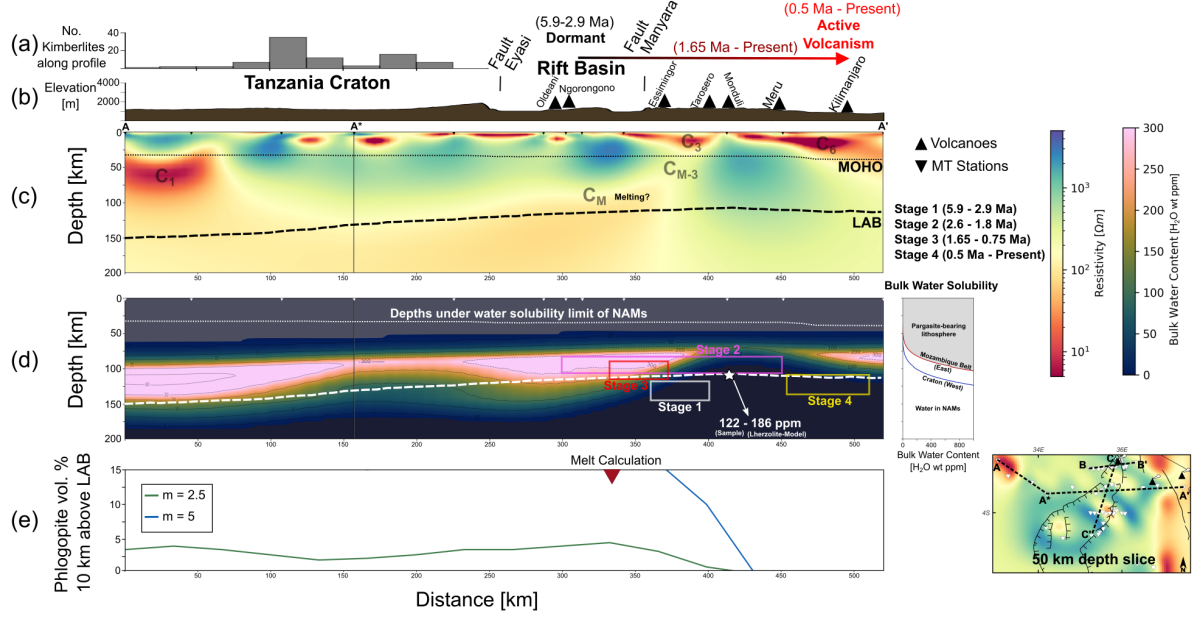


**Figure 6.** MT slice along the A - A' profile and other estimated and catalogued properties. (a) Histogram showing the number of kimberlites within the 50 km proximity of the profile. Since there are no kimberlites within the Eastern portion, the profile is cut after Fault Eyasi. (b) Elevation along the profile. (c) MT slice along the profile, also showing LAB and MOHO acquired from Afonso et al. (2022). (d) Water content estimation along the profile, where the shaded regions with white indicate the places below the water solubility limit. Melted lithosphere portions at different stages (Stage 1 - 4) envisioned by the study of Mana et al. (2015) are indicated on the slice. Bulk water solubility limits calculated with Padrón-Navarta & Hermann (2017) for end-member Craton and Mozambique Belt geotherms are also shown on the right-hand side of the figure. (e) Estimated volumetric abundances of phlogopite (% 0.52 F) to fit the MT model 10 km below the LAB with different interconnection ( $m$ ) values.



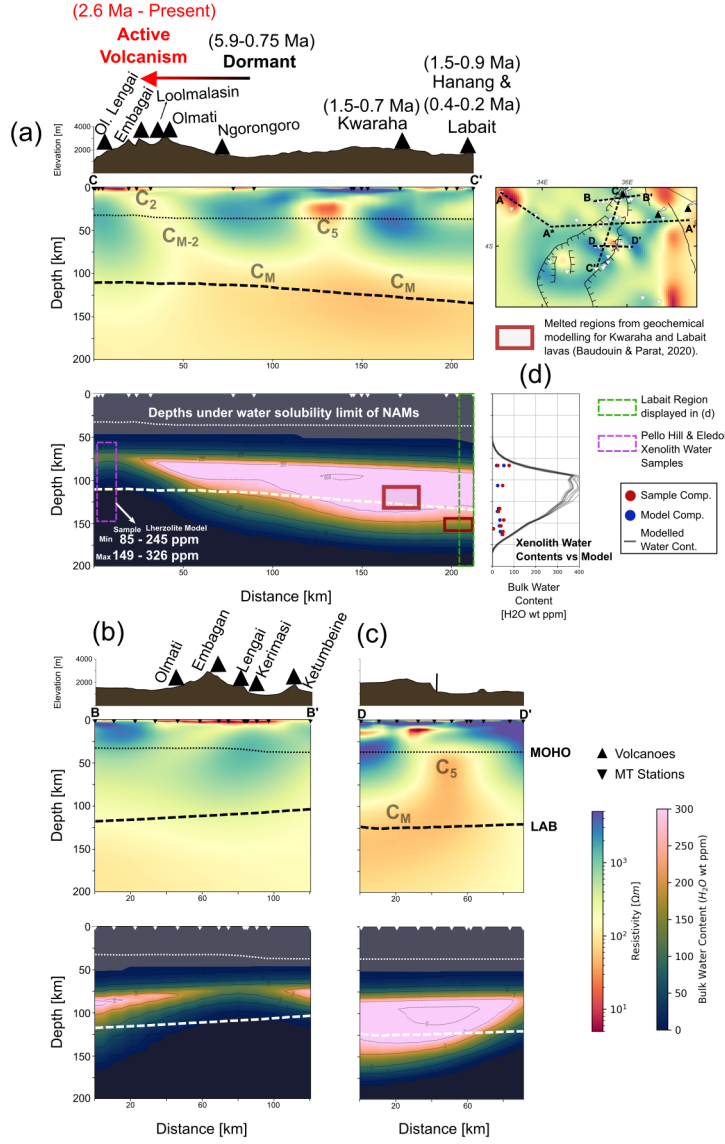


**Figure 7.** MT and estimated bulk water content slices along (a) C - C', (b) B - B', and (c) D - D' profiles. Melted regions envisioned by the study of Baudouin & Parat (2020) for Kwaraha and Labait Volcanoes are indicated with red water content slice of (a). (d) Modelled water content profiles around the Labait Volcano compared to xenolith water contents Hui et al. (2015). We used the orthopyroxene water measurements to convert them to bulk water contents with composition used in water models (blue circles) and individual compositions for each sample indicated in the study.

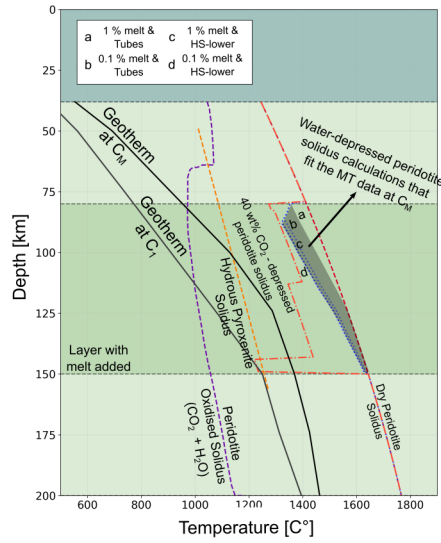


**Figure 8.** Geotherm near conductor  $C_M$  at the rift-axis alongside different peridotite and pyroxenite solidus curves. These solidus curves include Dry peridotite solidus (Hirschmann et al., 2009),  $H_2O$ -depressed peridotite solidus fitting the conductivity at  $C_M$  (Hirschmann et al., 2009) with scenarios varying with different melt contents and interconnection scenarios (see legend a-d); 40 wt %  $CO_2$  - depressed peridotite solidus (orange curve, Dasgupta et al., 2013); hydrous pyroxenite solidus (yellow curve, Foley et al., 2022),  $CO_2 + H_2O$  saturated peridotite (purple curve, Foley et al., 2009).

The dominant conclusion from numerous studies investigating the rheological response to rifting in this region is not that it is unusual that the Tanzanian Craton is stable, but rather that it is instead surprising that the adjacent lithosphere of the Eastern and Western Branches is rifting (e.g., Behn et al., 2006; Buck, 2006; O'Donnell et al., 2016; Koptev et al., 2016). The stresses in the region are tensional and primarily derived from gradients in the gravitational potential associated with the uplift of the East African Plateau (Stamps et al., 2014; Craig et al., 2011; Rajaonarison et al., 2021). These stresses provide only a fraction of the stress theoretically needed to rift thick ( $>100$  km thickness) and melt-free lithosphere. Adding to this challenge, as pointed out by Selway et al. (2014) and Selway (2015) and confirmed in the results shown here, is that much of the lithospheric mantle beneath the Eastern Branch is dehydrated. Since water content in olivine is one of the major controls on mantle rheology, (e.g., Hirth & Kohlstedt, 2003), higher water contents in the cratonic mantle should, all else being equal, make it weaker than the Eastern Branch lithospheric mantle. Selway (2015) suggested that small grain sizes in the Eastern Branch lithosphere, which may still remain as a scar from Pan-African deformation, could contribute to weakening the Eastern Branch lithosphere and could outweigh the impact of water content (e.g., Ramirez et al., 2022). Mantle xenoliths from the volcanoes along the rift zone (Pello Hill and Elodoi) do indeed dominantly have porphyroclastic textures with smaller olivine grain sizes (0.4 to 2 mm Baptiste et al., 2015). In the less developed parts of the rift zone towards the south (Labait Volcano), porphyroclastic textures only exist in the samples with the highest equilibrium temperatures ( $1450^\circ\text{C}$ ), whereas larger grain sizes (5-15 mm) were observed in lithospheric samples (Vauchez et al., 2005). Xenolith samples from Lashaine, east of the rift valley, show similar textures to lithospheric samples from Labait (Baptiste et al., 2015). Even though they occur in close proximity in space and time to Lashaine, Olmani xenoliths consist of porphyroclastic to coarse textures with small grain sizes, suggesting that the area east of the rift valley experienced heterogeneous distribution of stress and, therefore, that localised deformation might have occurred (Baptiste et al., 2015).

Although fine grain sizes in the rift zone will reduce mantle viscosity, most calculations suggest that the East African lithosphere should still be too strong to rift in the presence of the available stresses (e.g., O'Donnell et al., 2016). Instead, the presence of melt is the most effective mechanism to reduce the strength of the Tanzanian lithosphere enough that it deforms (e.g., Buck, 2006; O'Donnell et al., 2016; Reiss et al., 2022). Correlations between the timing of volcanism and faulting in the NTD (e.g., Le Gall et al., 2008) lend support to the idea that the East African Rift lithosphere is weakened by active magmatism. The MT results presented here can improve our understanding of the distribution of melt within the lithospheric mantle of the NTD and of the likely development of large-scale deformation. Within the cratonic mantle lithosphere, although resistivities are low, the lack of high-volume Cenozoic surface volcanism and the high seismic velocities suggest that there is no melt present and that the low resistivities are attributable to solid-state causes. Within the Eastern Branch, despite the generally higher resistivities, the recent and active volcanism (Mana et al., 2015), low seismic velocities (Clutier et al., 2021; Tiberi et al., 2019), and high seismic attenuation (Reiss et al., 2022) suggest that melt is present in the lithosphere. The seismic and MT observations can be reconciled if melt is present in a sufficiently small volume that it resides in triple junctions but does not coat grain boundaries (e.g., Selway & O'Donnell, 2019) and the mantle conductor  $C_M$  (Fig. 6) may indicate regions with slightly higher and more interconnected melt concentrations.

Geochemical investigations of magmatism in the East Africa Rift suggest that thermal input has occurred in pulses (e.g., Rooney, 2020). During later thermal pulses, portions of the lithospheric mantle that were metasomatised in earlier pulses are progressively melted until, eventually, the lithospheric mantle is depleted and magmas are sourced from the sub-lithospheric mantle (e.g., Rooney, 2020; Mana et al., 2015). The relatively dehydrated nature of the lithospheric mantle in the Mozambique Belt suggests that this process is already well-developed. Magma currently within the lithospheric mantle may contain significant sub-lithospheric material (Muirhead et al., 2020) and may be scavenging any remaining

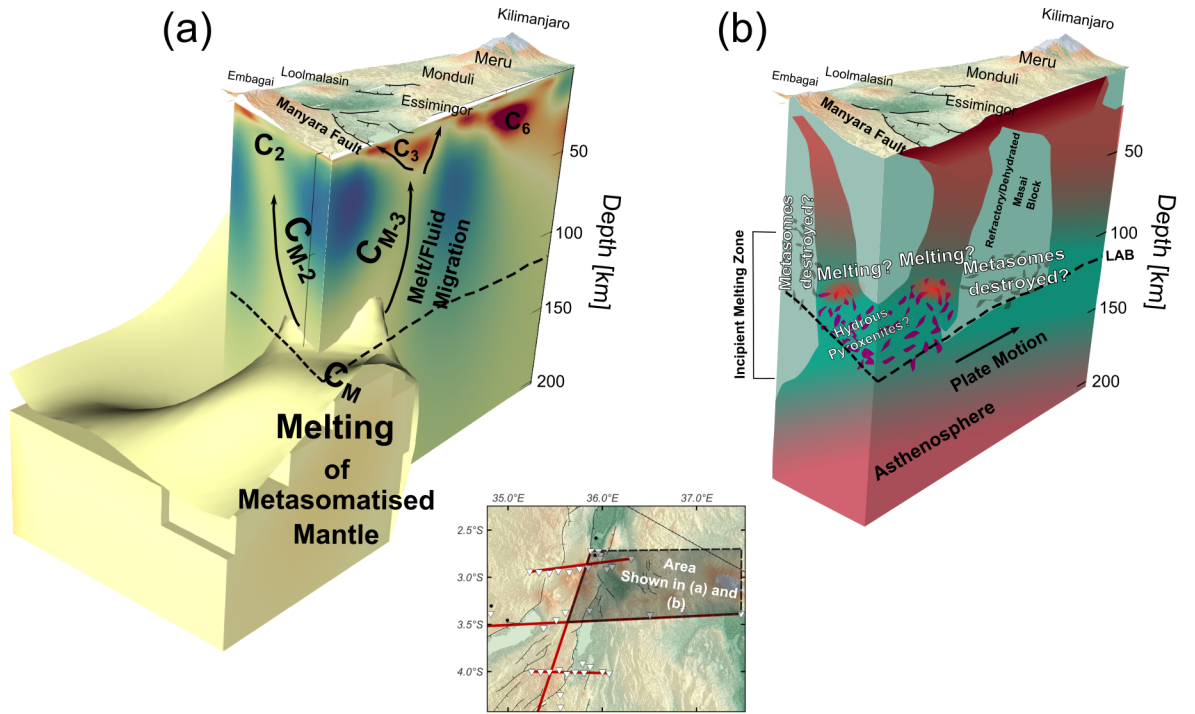


**Figure 9.** 3D representation of the MT model in the eastern portion of the area (see shaded area in the inset map) structured with (a) 3D MT model slices, and (b) the interpretive sketch dependent on the results of this study.

metasomatised material from the lithosphere (Mana et al., 2015). This dehydration of the lithosphere suggests that, unless there are large future thermal pulses to inject significant volumes of sub-lithospheric melt into the Eastern Branch lithospheric mantle, future volcanism in this part of the Eastern Branch may be limited. Given that magma is a primary control on lithospheric strength, this may mean that the extent of rifting in the Eastern Branch will also be limited. The outlook for rifting and deformation would differ if the plume were to migrate towards parts of the lithospheric mantle that still contain metasomatic phases, including the adjacent cratonic lithosphere, inducing redox melting (Muirhead et al., 2020; Foley & Fischer, 2017). The effect of grain sizes, hydrolytic weakening of olivine, structural inheritance and existence of melt should be tested with geodynamic modelling using the results of this study to further constrain the mechanisms accommodating rifting in this region.

## 5 Conclusions

Newly developed 3D MT models of the Northern Tanzanian Divergence are subjected to quantified interpretations. The most important conclusions of this study are:

- The cratonic region displays signs of a metasomatised lithosphere throughout, especially around the prominent conductor  $C_1$ . The large conductor  $C_1$  lies above the water solubility limit of NAMs, suggesting other minor conductive phases, particularly graphite and sulphides, might be responsible for its formation.
- Kimberlites on the craton appear on the metasomatised/hydrated portions of the lithosphere and avoid the prominent conductor  $C_1$ , which aligns with the previously observed relationship between electrical conductivity and kimberlite distribution around the world (Özaydın & Selway, 2022).
- The garnet xenocryst section demonstrates a layered lithosphere where the mantle below  $\sim 160$  km is abundantly melt-metasomatised, which matches mantle xenolith observations from the region (e.g., Lee & Rudnick, 1999). This boundary also coincides with geophysical interpretations of the current LAB and displays a transition from a hydrated/metasomatised to a dry lithosphere.
- The rift zone is electrically heterogeneous, where primary conductors follow the fault zones. In the deeper rift zone, the conductor  $C_M$  appears, which correlates well with the suggested melt-bearing regions from seismic tomography studies (Clutier et al., 2021; Reiss et al., 2022). As well as melt, the conductive nature of the region may indicate the presence of metasomes that are likely to reduce the solidus and induce melting in the presence of a thermal anomaly.
- The mantle beneath the northern rift zone (proximal to Oldoinyo Lengai) and the region spanning Mt Essimigor to Mt Kilimanjaro appears to be dehydrated. This might indicate that melting in these areas caused metasomes to be destroyed, and consequently the mantle to be dehydrated. The fact that mantle xenolith water contents also do not match the MT-derived water contents in these regions might indicate that the area has evolved significantly in composition since eruption of the xenoliths.
- The dehydrated nature of the Mozambique Belt suggests that rifting might be accommodated through melting of metasomes across the rift zone. In the absence of an enhanced thermal anomaly, the rifting in the Eastern Branch might be limited in future geological times.

## Open Research

We used the *ModEM* inversion code for 3D MT modelling, which can be accessed by contacting the developers <http://www.modem-geophysics.com/>. The quantified interpretations of the MT model were made by using the software *MATE* (Özaydın & Sel-

way, 2020), which can be found at <https://github.com/sinanozaydin/MATE>. The python library *Thermobar* is used to make thermobarometric calculations and garnet xenocryst analyses (Wieser et al., 2022), which can be found at <https://github.com/PennyWieser/Thermobar>. Phase tensor ellipses are generated using the python library *mtpy* (<https://github.com/MTgeophysics/mtpy>). Original MT model and data files, water model files can be found at <https://doi.org/10.5281/zenodo.8232221>.

## Acknowledgments

This study was financially supported by the Covid Recovery Fellowship scheme run by Macquarie University. All original MT data collection was supported by the government of Tanzania through the Tanzanian Commission for Science and Technology (COSTECH) and the Geological Survey of Tanzania. We are grateful for the generous assistance of the University of Dar es Salaam, local schools, residents and land-owners, and particularly Mr Mtelela Khalfan (UDSM), whose extraordinary skills, patience, good nature and hard work enabled these datasets to be collected.

## References

- Abers, G. A., & Hacker, B. R. (2016). A matlab toolbox and excel workbook for calculating the densities, seismic wave speeds, and major element composition of minerals and rocks at pressure and temperature. *Geochemistry, Geophysics, Geosystems*, 17(2), 616–624.
- Acocella, V. (2014). Structural control on magmatism along divergent and convergent plate boundaries: Overview, model, problems. *Earth-Science Reviews*, 136, 226–288.
- Afonso, J. C., Ben-Mansour, W., O'Reilly, S. Y., Griffin, W. L., Salajegheh, F., Foley, S. F., . . . others (2022). Thermochemical structure and evolution of cratonic lithosphere in central and southern africa. *Nature Geoscience*, 15(5), 405–410.
- Amante, C., & Eakins, B. W. (2009). Etopo1 1 arc-minute global relief model: procedures, data sources and analysis. noaa technical memorandum nesdis ngdc-24. *National Geophysical Data Center, NOAA*, 10(2009), V5C8276M.
- Aulbach, S., Lin, A.-B., Weiss, Y., & Yaxley, G. (2020). Wehrlites from continental mantle monitor the passage and degassing of carbonated melts. *Geochemical Perspective Letters*.
- Aulbach, S., Rudnick, R. L., & McDonough, W. F. (2011). Evolution of the lithospheric mantle beneath the east african rift in tanzania and its potential signatures in rift magmas. *Geological Society of America Special Papers*, 478, 105–125.
- Baptiste, V., Tommasi, A., Vauchez, A., Demouchy, S., & Rudnick, R. L. (2015). Deformation, hydration, and anisotropy of the lithospheric mantle in an active rift: Constraints from mantle xenoliths from the north tanzanian divergence of the east african rift. *Tectonophysics*, 639, 34–55.
- Baudouin, C., & Parat, F. (2020). Phlogopite-olivine nephelinites erupted during early stage rifting, north tanzanian divergence. *Frontiers in Earth Science*, 8, 277.
- Baudouin, C., Parat, F., Denis, C. M., & Mangasini, F. (2016). Nephelinite lavas at early stage of rift initiation (hanang volcano, north tanzanian divergence). *Contributions to Mineralogy and Petrology*, 171, 1–20.
- Behn, M. D., Buck, W. R., & Sacks, I. S. (2006). Topographic controls on dike injection in volcanic rift zones. *Earth and Planetary Science Letters*, 246(3-4), 188–196.
- Bell, D. R., Ihinger, P. D., & Rossman, G. R. (1995, jun). Quantitative analysis of trace OH in garnet and pyroxenes. *American Mineralogist*, 80(5-6), 465–474. doi: 10.2138/am-1995-5-607
- Booker, J. R. (2014). The magnetotelluric phase tensor: a critical review. *Surveys in Geophysics*, 35(1), 7–40.
- Boone, S. C., Kohn, B. P., Gleadow, A. J., Morley, C. K., Seiler, C., & Foster, D. A. (2019). Birth of the east african rift system: Nucleation of magmatism and strain in the turkana depression. *Geology*, 47(9), 886–890.



- Brune, S., Kolawole, F., Olive, J.-A., Stamps, D. S., Buck, W. R., Buitter, S. J. H., ... Shillington, D. J. (2023, March). Geodynamics of continental rift initiation and evolution. *Nature Reviews Earth & Environment*. doi: 10.1038/s43017-023-00391-3
- Buck, W. (2006). The role of magma in the development of the afro-arabian rift system. *Geological Society, London, Special Publications*, 259(1), 43–54.
- Chesley, J. T., Rudnick, R. L., & Lee, C.-T. (1999). Re-os systematics of mantle xenoliths from the east african rift: Age, structure, and history of the tanzanian craton. *Geochimica et Cosmochimica Acta*, 63(7-8), 1203–1217.
- Clutier, A., Gautier, S., & Tiberi, C. (2021). Hybrid local and teleseismic p-wave tomography in north tanzania: role of inherited structures and magmatism on continental rifting. *Geophysical Journal International*, 224(3), 1588–1606.
- Craig, T., Jackson, J., Priestley, K., & McKenzie, D. (2011). Earthquake distribution patterns in africa: their relationship to variations in lithospheric and geological structure, and their rheological implications. *Geophysical Journal International*, 185(1), 403–434.
- Dai, L., Hu, H., Jiang, J., Sun, W., Li, H., Wang, M., ... Saltas, V. (2020). An overview of the experimental studies on the electrical conductivity of major minerals in the upper mantle and transition zone. *Materials*, 13(2), 408.
- Dai, L., Hu, H., Sun, W., Li, H., Liu, C., & Wang, M. (2019). Influence of high conductive magnetite impurity on the electrical conductivity of dry olivine aggregates at high temperature and high pressure. *Minerals*, 9(1). doi: 10.3390/min9010044
- Dai, L., & Karato, S.-i. (2009a). Electrical conductivity of orthopyroxene: Implications for the water content of the asthenosphere. *Proceedings of the Japan Academy, Series B*, 85(10), 466–475. doi: 10.2183/pjab.85.466
- Dai, L., & Karato, S.-i. (2009b). Electrical conductivity of pyrope-rich garnet at high temperature and high pressure. *Physics of the Earth and Planetary Interiors*, 176(1-2), 83–88. doi: 10.1016/j.pepi.2009.04.002
- Daly, M., Chorowicz, J., & Fairhead, J. (1989). Rift basin evolution in africa: the influence of reactivated steep basement shear zones. *Geological Society, London, Special Publications*, 44(1), 309–334.
- Dambly, M., Samrock, F., Grayver, A., & Saar, M. O. (2023). Insights on the interplay of rifting, transcrustal magmatism and formation of geothermal resources in the central segment of the ethiopian rift revealed by 3-d magnetotelluric imaging. *Journal of Geophysical Research: Solid Earth*, e2022JB025849.
- Dasgupta, R., Mallik, A., Tsuno, K., Withers, A. C., Hirth, G., & Hirschmann, M. M. (2013). Carbon-dioxide-rich silicate melt in the earth’s upper mantle. *Nature*, 493(7431), 211–215.
- Demouchy, S., & Alard, O. (2021). Hydrogen, trace, and ultra-trace element distribution in natural olivines. *Contributions to Mineralogy and Petrology*, 176(4), 26.
- Demouchy, S., & Bolfan-Casanova, N. (2016). Distribution and transport of hydrogen in the lithospheric mantle: A review. *Lithos*, 240, 402–425.
- Demouchy, S., Shcheka, S., Denis, C. M., & Thoraval, C. (2017). Subsolidus hydrogen partitioning between nominally anhydrous minerals in garnet-bearing peridotite. *American Mineralogist*, 102(9), 1822–1831. doi: 10.2138/am-2017-6089
- Denis, C. M., Demouchy, S., & Alard, O. (2018). Heterogeneous hydrogen distribution in orthopyroxene from veined mantle peridotite (san carlos, arizona): Impact of melt-rock interactions. *Lithos*, 302, 298–311.
- Ebinger, C. (2012). Evolution of the cenozoic east african rift system: cratons, plumes and continental breakup. In *Regional geology and tectonics: Phanerozoic rift systems and sedimentary basins* (Vol. 1, pp. 132–162). Elsevier Amsterdam.
- Ebinger, C., Djomani, Y. P., Mbede, E., Foster, A., & Dawson, J. (1997). Rifting archaean lithosphere: the eyasi-manyara-natron rifts, east africa. *Journal of the Geological Society*, 154(6), 947–960.
- Ebinger, C., & Sleep, N. (1998). Cenozoic magmatism throughout east africa resulting from impact of a single plume. *Nature*, 395(6704), 788–791.

- Emry, E. L., Shen, Y., Nyblade, A. A., Flinders, A., & Bao, X. (2019). Upper mantle earth structure in africa from full-wave ambient noise tomography. *Geochemistry, Geophysics, Geosystems*, *20*(1), 120–147.
- Foley, S. F. (1992). Vein-plus-wall-rock melting mechanisms in the lithosphere and the origin of potassic alkaline magmas. *Lithos*, *28*(3-6), 435–453.
- Foley, S. F., Ezad, I. S., van der Laan, S. R., & Pertermann, M. (2022). Melting of hydrous pyroxenites with alkali amphiboles in the continental mantle: 1. melting relations and major element compositions of melts. *Geoscience Frontiers*, *13*(4), 101380.
- Foley, S. F., & Fischer, T. P. (2017). An essential role for continental rifts and lithosphere in the deep carbon cycle. *Nature Geoscience*, *10*(12), 897–902.
- Foley, S. F., Link, K., Tiberindwa, J., & Barifaijo, E. (2012). Patterns and origin of igneous activity around the tanzanian craton. *Journal of African Earth Sciences*, *62*(1), 1–18.
- Foley, S. F., & Pintér, Z. (2018). Primary melt compositions in the earth’s mantle. In *Magmas under pressure* (pp. 3–42). Elsevier.
- Foley, S. F., Yaxley, G., Rosenthal, A., Buhre, S., Kiseeva, E., Rapp, R., & Jacob, D. (2009). The composition of near-solidus melts of peridotite in the presence of co<sub>2</sub> and h<sub>2</sub>o between 40 and 60 kbar. *Lithos*, *112*, 274–283.
- Gardés, E., Gaillard, F., & Tarits, P. (2014, dec). Toward a unified hydrous olivine electrical conductivity law. *Geochemistry, Geophysics, Geosystems*, *15*(12), 4984–5000. doi: 10.1002/2014GC005496
- Giuliani, A., & Pearson, D. G. (2019). Kimberlites: from deep earth to diamond mines. *Elements: An International Magazine of Mineralogy, Geochemistry, and Petrology*, *15*(6), 377–380.
- Glover, P. W. (2010). A generalized archie’s law for n phases. *Geophysics*, *75*(6), E247–E265.
- Grantham, G., Maboko, M., & Eglington, B. (2003). A review of the evolution of the mozambique belt and implications for the amalgamation and dispersal of roдинia and gondwana. *Geological Society, London, Special Publications*, *206*(1), 401–425.
- Grégoire, M., Bell, D., & Le Roex, A. (2002). Trace element geochemistry of phlogopite-rich mafic mantle xenoliths: their classification and their relationship to phlogopite-bearing peridotites and kimberlites revisited. *Contributions to Mineralogy and Petrology*, *142*, 603–625.
- Griffin, W. L., Fisher, N. I., Friedman, J. H., O’Reilly, S. Y., & Ryan, C. G. (2002). Cr-pyropite garnets in the lithospheric mantle 2. Compositional populations and their distribution in time and space. *Geochemistry, Geophysics, Geosystems*, *3*(12), 1–35. doi: 10.1029/2002gc000298
- Griffin, W. L., O’Reilly, S. Y., Natapov, L. M., & Ryan, C. G. (2003). The evolution of lithospheric mantle beneath the Kalahari Craton and its margins. *Lithos*, *71*(2-4), 215–241. doi: 10.1016/j.lithos.2003.07.006
- Griffin, W. L., Ryan, C., O’Reilly, S., Nixon, P., & Win, T. (1991). Trace elements in garnets from tanzanian kimberlites: Relation to diamond content and tectonic setting. In *International kimberlite conference: Extended abstracts* (Vol. 5, pp. 145–147).
- Grütter, H. S., Gurney, J. J., Menzies, A. H., & Winter, F. (2004). An updated classification scheme for mantle-derived garnet, for use by diamond explorers. *Lithos*, *77*(1-4), 841–857.
- Hansen, S. E., Nyblade, A. A., & Benoit, M. H. (2012). Mantle structure beneath africa and arabia from adaptively parameterized p-wave tomography: Implications for the origin of cenozoic afro-arabian tectonism. *Earth and Planetary Science Letters*, *319*, 23–34.
- Hasterok, D., & Chapman, D. S. (2011). Heat production and geotherms for the continental lithosphere. *Earth and Planetary Science Letters*, *307*(1-2), 59–70. doi: 10.1016/j.epsl.2011.04.034
- Heinson, G., Didana, Y., Soeffky, P., Thiel, S., & Wise, T. (2018). The crustal geophysical signature of a world-class magmatic mineral system. *Scientific reports*, *8*(1), 10608.
- Hirschmann, M. M., Tenner, T., Aubaud, C., & Withers, A. (2009). Dehydration melting of nominally anhydrous mantle: The primacy of partitioning. *Physics of the Earth and*

- Planetary Interiors, 176(1-2), 54–68.
- Hirth, G., & Kohlstedt, D. (2003). Rheology of the upper mantle and the mantle wedge: A view from the experimentalists. *Geophysical monograph-american geophysical union*, 138, 83–106.
- Hofmann, C., Courtillot, V., Feraud, G., Rochette, P., Yirgu, G., Ketefo, E., & Pik, R. (1997). Timing of the ethiopian flood basalt event and implications for plume birth and global change. *Nature*, 389(6653), 838–841.
- Hübert, J., Whaler, K., & Fisseha, S. (2018). The electrical structure of the central main ethiopian rift as imaged by magnetotellurics: implications for magma storage and pathways. *Journal of Geophysical Research: Solid Earth*, 123(7), 6019–6032.
- Hui, H., Peslier, A. H., Rudnick, R. L., Simonetti, A., & Neal, C. R. (2015). Plume-cratonic lithosphere interaction recorded by water and other trace elements in peridotite xenoliths from the labait volcano, tanzania. *Geochemistry, Geophysics, Geosystems*, 16(6), 1687–1710.
- Kelbert, A., Meqbel, N., Egbert, G. D., & Tandon, K. (2014). ModEM: A modular system for inversion of electromagnetic geophysical data. *Computers and Geosciences*, 66, 40–53. doi: 10.1016/j.cageo.2014.01.010
- Kirkby, A., Czarnota, K., Huston, D. L., Champion, D. C., Doublier, M. P., Bedrosian, P. A., ... Heinson, G. (2022). Lithospheric conductors reveal source regions of convergent margin mineral systems. *Scientific Reports*, 12(1), 1–10.
- Kirkby, A., & Doublier, M. P. (2022). Synthetic magnetotelluric modelling of a regional fault network—implications for survey design and interpretation. *Exploration Geophysics*, 1–12.
- Koornneef, J. M., Davies, G. R., Döpp, S. P., Vukmanovic, Z., Nikogosian, I. K., & Mason, P. R. (2009). Nature and timing of multiple metasomatic events in the sub-cratonic lithosphere beneath labait, tanzania. *Lithos*, 112, 896–912.
- Koptev, A., Burov, E., Calais, E., Leroy, S., Gerya, T., Guillou-Frottier, L., & Cloetingh, S. (2016). Contrasted continental rifting via plume-craton interaction: Applications to central east african rift. *Geoscience Frontiers*, 7(2), 221–236.
- Lee, C., & Rudnick, R. (1999). Compositionally stratified cratonic lithosphere: petrology and geochemistry of peridotite xenoliths from the labait tuff cone, tanzania. In *Proceedings of the 7th international kimberlite conference* (pp. 503–521).
- Le Gall, B., Nonnotte, P., Rolet, J., Benoit, M., Guillou, H., Mousseau-Nonnotte, M., ... Deverchère, J. (2008). Rift propagation at craton margin.: Distribution of faulting and volcanism in the north tanzanian divergence (east africa) during neogene times. *Tectonophysics*, 448(1-4), 1–19.
- Lehnert, K., Su, Y., Langmuir, C., Sarbas, B., & Nohl, U. (2000). A global geochemical database structure for rocks. *Geochemistry, Geophysics, Geosystems*, 1(5).
- Li, Y., Jiang, H., & Yang, X. (2017). Fluorine follows water: Effect on electrical conductivity of silicate minerals by experimental constraints from phlogopite. *Geochimica et Cosmochimica Acta*, 217, 16–27.
- Liu, H., Zhu, Q., & Yang, X. (2019). Electrical conductivity of oh-bearing omphacite and garnet in eclogite: the quantitative dependence on water content. *contributions to mineralogy and Petrology*, 174(7), 1–15.
- Maboko, M. A. (2000). Nd and sr isotopic investigation of the archaean–proterozoic boundary in north eastern tanzania: constraints on the nature of neoproterozoic tectonism in the mozambique belt. *Precambrian Research*, 102(1-2), 87–98.
- Mana, S., Furman, T., Turrin, B. D., Feigenson, M. D., & Swisher III, C. C. (2015). Magmatic activity across the east african north tanzanian divergence zone. *Journal of the Geological Society*, 172(3), 368–389.
- Manya, S., Kobayashi, K., Maboko, M. A., & Nakamura, E. (2006). Ion microprobe zircon u–pb dating of the late archaean metavolcanics and associated granites of the musoma-mara greenstone belt, northeast tanzania: Implications for the geological evolution of the tanzania craton. *Journal of African Earth Sciences*, 45(3), 355–366.

- Mattsson, H. B., Nandedkar, R. H., & Ulmer, P. (2013). Petrogenesis of the melilititic and nephelinitic rock suites in the lake natron–engaruka monogenetic volcanic field, northern tanzania. *Lithos*, 179, 175–192.
- Meju, M. A., & Sakkas, V. (2007). Heterogeneous crust and upper mantle across southern kenya and the relationship to surface deformation as inferred from magnetotelluric imaging. *Journal of Geophysical Research: Solid Earth*, 112(B4).
- Muhongo, S., Kröner, A., & Nemchin, A. (2001). Single zircon evaporation and shrimp ages for granulite-facies rocks in the mozambique belt of tanzania. *The Journal of Geology*, 109(2), 171–189.
- Muirhead, J. D., Fischer, T. P., Oliva, S. J., Laizer, A., van Wijk, J., Currie, C. A., ... others (2020). Displaced cratonic mantle concentrates deep carbon during continental rifting. *Nature*, 582(7810), 67–72.
- Muirhead, J. D., & Kattenhorn, S. A. (2018). Activation of preexisting transverse structures in an evolving magmatic rift in east africa. *Journal of Structural Geology*, 106, 1–18.
- Mulibo, G. D., & Nyblade, A. A. (2013a). Mantle transition zone thinning beneath eastern africa: Evidence for a whole-mantle superplume structure. *Geophysical Research Letters*, 40(14), 3562–3566.
- Mulibo, G. D., & Nyblade, A. A. (2013b). The p and s wave velocity structure of the mantle beneath eastern africa and the african superplume anomaly. *Geochemistry, Geophysics, Geosystems*, 14(8), 2696–2715.
- Naif, S., Selway, K., Murphy, B. S., Egbert, G., & Pommier, A. (2021). Electrical conductivity of the lithosphere-asthenosphere system. *Physics of the Earth and Planetary Interiors*, 313(2021), 10661.
- Novella, D., Frost, D. J., Hauri, E. H., Bureau, H., Raepsaet, C., & Roberge, M. (2014). The distribution of H<sub>2</sub>O between silicate melt and nominally anhydrous peridotite and the onset of hydrous melting in the deep upper mantle. *Earth and Planetary Science Letters*, 400, 1–13. doi: 10.1016/j.epsl.2014.05.006
- Nyblade, A. A. (1997). Heat flow across the east african plateau. *Geophysical Research Letters*, 24(16), 2083–2086.
- O'Donnell, J., Selway, K., Nyblade, A. A., Brazier, R., Tahir, N. E., & Durrheim, R. (2016). Thick lithosphere, deep crustal earthquakes and no melt: a triple challenge to understanding extension in the western branch of the east african rift. *Geophysical Journal International*, 204(2), 985–998.
- O'Reilly, S., & Griffin, W. L. (1996). 4-d lithosphere mapping: methodology and examples. *Tectonophysics*, 262(1-4), 3–18.
- Özaydın, S., & Selway, K. (2022). The relationship between kimberlitic magmatism and electrical conductivity anomalies in the mantle. *Geophysical Research Letters*, e2022GL099661.
- Özaydın, S., Selway, K., & Griffin, W. L. (2021). Are xenoliths from southwestern kaapvaal craton representative of the broader mantle? constraints from magnetotelluric modeling. *Geophysical Research Letters*, 48(11), e2021GL092570.
- Özaydın, S., Selway, K., Griffin, W. L., & Moorkamp, M. (2022). Probing the southern african lithosphere with magnetotellurics: 2. linking electrical conductivity, composition, and tectonomagmatic evolution. *Journal of Geophysical Research: Solid Earth*, 127(3), e2021JB023105.
- Özaydın, S., & Selway, K. (2020). MATE: An analysis tool for the interpretation of magnetotelluric models of the mantle. *Geochemistry, Geophysics, Geosystems*, 1–26. doi: 10.1029/2020gc009126
- O'Donnell, J., Adams, A., Nyblade, A., Mulibo, G., & Tugume, F. (2013). The uppermost mantle shear wave velocity structure of eastern africa from rayleigh wave tomography: Constraints on rift evolution. *Geophysical Journal International*, 194(2), 961–978.
- Padrón-Navarta, J. A., & Hermann, J. (2017). A Subsolidus Olivine Water Solubility Equation for the Earth's Upper Mantle. *Journal of Geophysical Research: Solid Earth*, 122(12), 9862–9880. doi: 10.1002/2017JB014510

- Paterson, M. (1982). The determination of hydroxyl by infrared absorption in quartz, silicate glasses and similar materials. *Bulletin de minéralogie*, 105(1), 20–29.
- Peslier, A., Woodland, A., Bell, D., Lazarov, M., & Lapen, T. (2012). Metasomatic control of water contents in the kaapvaal cratonic mantle. *Geochimica et Cosmochimica Acta*, 97, 213–246.
- Pintér, Z., Foley, S. F., Yaxley, G. M., Rosenthal, A., Rapp, R. P., Lanati, A. W., & Rushmer, T. (2021). Experimental investigation of the composition of incipient melts in upper mantle peridotites in the presence of  $\text{CO}_2$  and  $\text{H}_2\text{O}$ . *Lithos*, 396, 106224.
- Plasman, M., Hautot, S., Tarits, P., Gautier, S., Tiberi, C., Le Gall, B., ... Gama, R. (2019). Lithospheric structure of a transitional magmatic to amagmatic continental rift system—insights from magnetotelluric and local tomography studies in the north tanzanian divergence, east african rift. *Geosciences*, 9(11), 462.
- Rajaonarison, T. A., Stamps, D. S., & Naliboff, J. (2021). Role of lithospheric buoyancy forces in driving deformation in east africa from 3d geodynamic modeling. *Geophysical Research Letters*, 48(6), e2020GL090483.
- Ramirez, F. D. C., Selway, K., Conrad, C. P., & Lithgow-Bertelloni, C. (2022). Constraining upper mantle viscosity using temperature and water content inferred from seismic and magnetotelluric data. *Journal of Geophysical Research: Solid Earth*, 127(8), e2021JB023824.
- Reiss, M., De Siena, L., & Muirhead, J. D. (2022). The interconnected magmatic plumbing system of the natron rift. *Geophysical Research Letters*, 49(15), e2022GL098922.
- Ritsema, J., Heijst, H. J. v., & Woodhouse, J. H. (1999). Complex shear wave velocity structure imaged beneath africa and iceland. *Science*, 286(5446), 1925–1928.
- Robertson, K., Heinson, G., & Thiel, S. (2016). Lithospheric reworking at the proterozoic–phanerozoic transition of australia imaged using auslamp magnetotelluric data. *Earth and Planetary Science Letters*, 452, 27–35.
- Rooney, T. O. (2020). The cenozoic magmatism of east africa: part iii—rifting of the craton. *Lithos*, 360, 105390.
- Rooney, T. O., Herzberg, C., & Bastow, I. D. (2012). Elevated mantle temperature beneath east africa. *Geology*, 40(1), 27–30.
- Ryan, C. G., Griffin, W. L., & Pearson, N. J. (1996). Garnet geotherms: Pressure-temperature data from cr-pyrope garnet xenocrysts in volcanic rocks. *Journal of Geophysical Research: Solid Earth*, 101(B3), 5611–5625.
- Sanislav, I. V., Kolling, S. L., Brayshaw, M., Cook, Y. A., Dirks, P. H., Blenkinsop, T. G., ... Ruhega, R. (2015). The geology of the giant nyankanga gold deposit, geita greenstone belt, tanzania. *Ore Geology Reviews*, 69, 1–16. doi: <https://doi.org/10.1016/j.oregeorev.2015.02.002>
- Selway, K. (2014). On the causes of electrical conductivity anomalies in tectonically stable lithosphere. *Surveys in Geophysics*, 35(1), 219–257.
- Selway, K. (2015). Negligible effect of hydrogen content on plate strength in east africa. *Nature Geoscience*, 8(7), 543–546.
- Selway, K., & O'Donnell, J. (2019). A small, unextractable melt fraction as the cause for the low velocity zone. *Earth and Planetary Science Letters*, 517, 117–124.
- Selway, K., Yi, J., & Karato, S.-I. (2014). Water content of the tanzanian lithosphere from magnetotelluric data: Implications for cratonic growth and stability. *Earth and Planetary Science Letters*, 388, 175–186.
- Stachel, T., Harris, J. W., & Brey, G. P. (1998). Rare and unusual mineral inclusions in diamonds from mwadui, tanzania. *Contributions to Mineralogy and Petrology*, 132(1), 34–47.
- Stamps, D., Flesch, L., Calais, E., & Ghosh, A. (2014). Current kinematics and dynamics of africa and the east african rift system. *Journal of Geophysical Research: Solid Earth*, 119(6), 5161–5186.
- Stern, R. J. (1994). Arc assembly and continental collision in the neoproterozoic east african orogen: implications for the consolidation of gondwanaland. *Annual review of earth and*



- 950 *planetary sciences*, 22(1), 319–351.
- 951 Ten Grotenhuis, S. M., Drury, M. R., Spiers, C. J., & Peach, C. J. (2005). Melt distribution  
952 in olivine rocks based on electrical conductivity measurements. *Journal of Geophysical*  
953 *Research: Solid Earth*, 110(B12).
- 954 Thomas, R. J., Spencer, C., Bushi, A. M., Baglow, N., Boniface, N., de Kock, G., ...  
955 others (2016). Geochronology of the central tanzania craton and its southern and eastern  
956 orogenic margins. *Precambrian Research*, 277, 47–67.
- 957 Tiberi, C., Gautier, S., Ebinger, C., Roecker, S., Plasman, M., Albaric, J., ... others (2019).  
958 Lithospheric modification by extension and magmatism at the craton-orogenic boundary:  
959 North tanzania divergence, east africa. *Geophysical Journal International*, 216(3), 1693–  
960 1710.
- 961 Tommasi, A., & Vauchez, A. (2001). Continental rifting parallel to ancient collisional belts:  
962 an effect of the mechanical anisotropy of the lithospheric mantle. *Earth and Planetary*  
963 *Science Letters*, 185(1-2), 199–210.
- 964 Vauchez, A., Dineur, F., & Rudnick, R. (2005). Microstructure, texture and seismic  
965 anisotropy of the lithospheric mantle above a mantle plume: Insights from the labait  
966 volcano xenoliths (tanzania). *Earth and Planetary Science Letters*, 232(3-4), 295–314.
- 967 Wang, Y.-F., Qin, J.-Y., Soustelle, V., Zhang, J.-F., & Xu, H.-J. (2021). Pyroxene does not  
968 always preserve its source hydrogen concentration: Clues from some peridotite xenoliths.  
969 *Geochimica et Cosmochimica Acta*, 292, 382–408.
- 970 Wieser, P., Petrelli, M., Lubbers, J., Wieser, E., Ozaydin, S., Kent, A., & Till, C. (2022).  
971 Thermobar: an open-source python3 tool for thermobarometry and hygrometry. *Vol-*  
972 *canica*, 5(2), 349–384.
- 973 Withers, A. C., Bureau, H., Raepsaet, C., & Hirschmann, M. M. (2012). Calibration of  
974 infrared spectroscopy by elastic recoil detection analysis of H in synthetic olivine. *Chemical*  
975 *Geology*, 334, 92–98. doi: 10.1016/j.chemgeo.2012.10.002
- 976 Yang, Y., Ingrin, J., Xia, Q., & Liu, W. (2019). Nature of hydrogen defects in clinopyroxenes  
977 from room temperature up to 1000 c: Implication for the preservation of hydrogen in the  
978 upper mantle and impact on electrical conductivity. *American mineralogist*, 104(1), 79–  
979 93.



Figure 1.

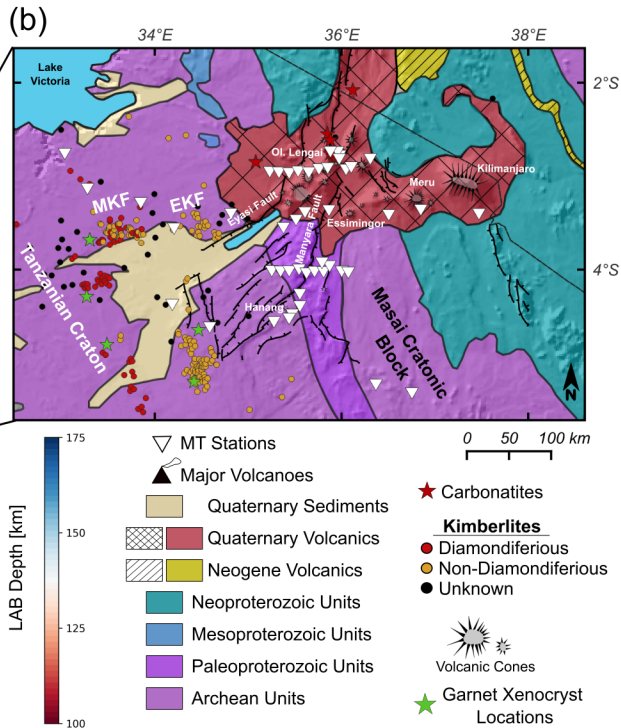
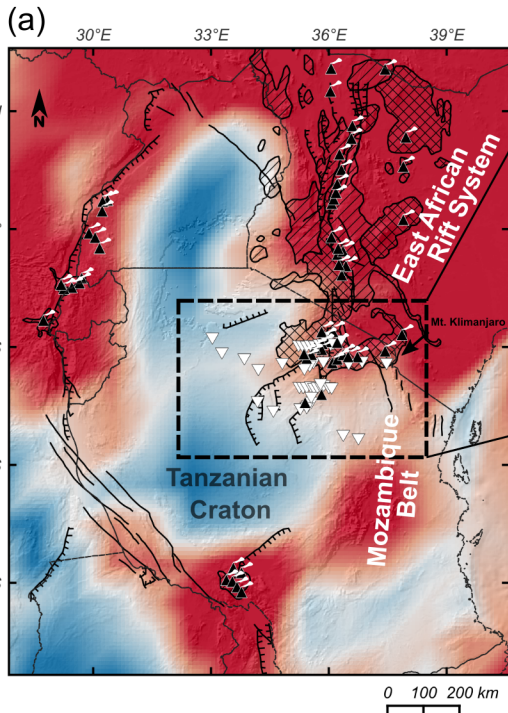


Figure 2.

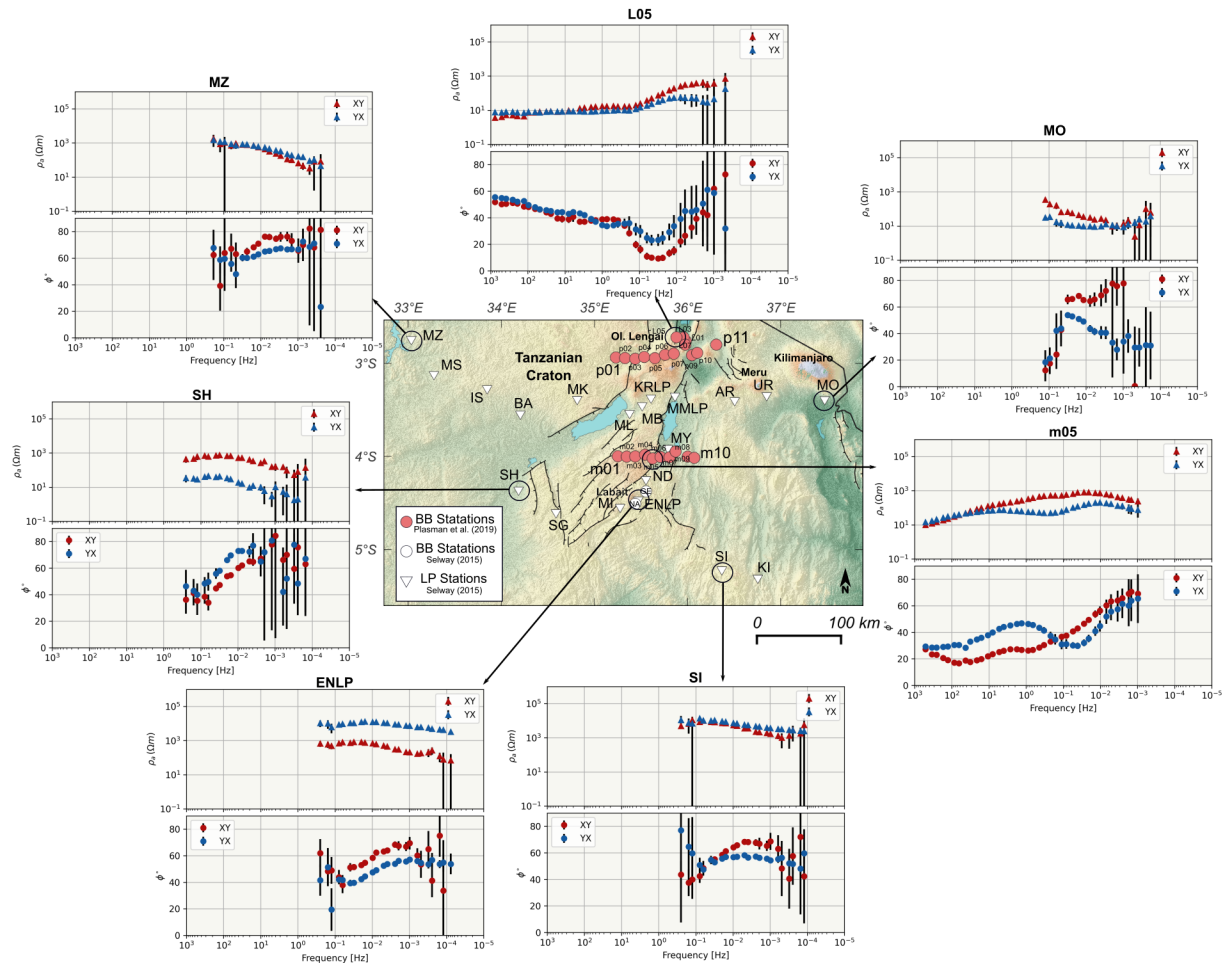


Figure 3.



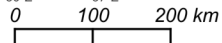
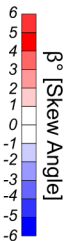
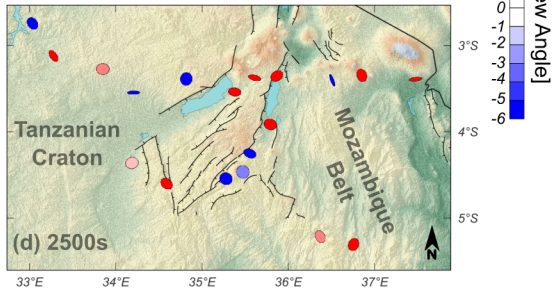
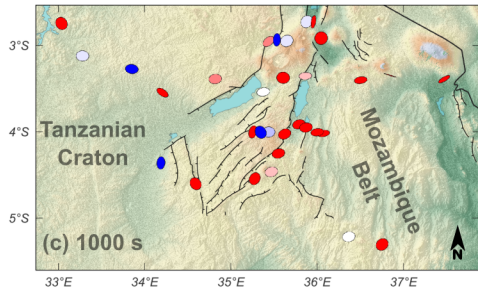
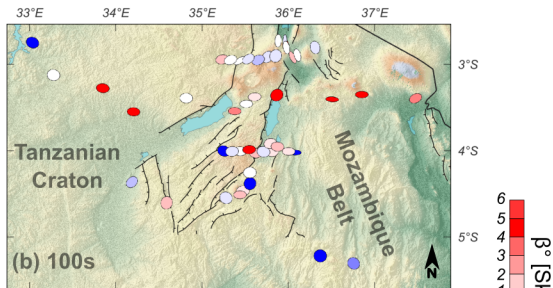
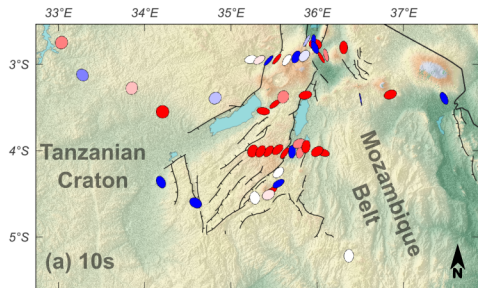


Figure 4.

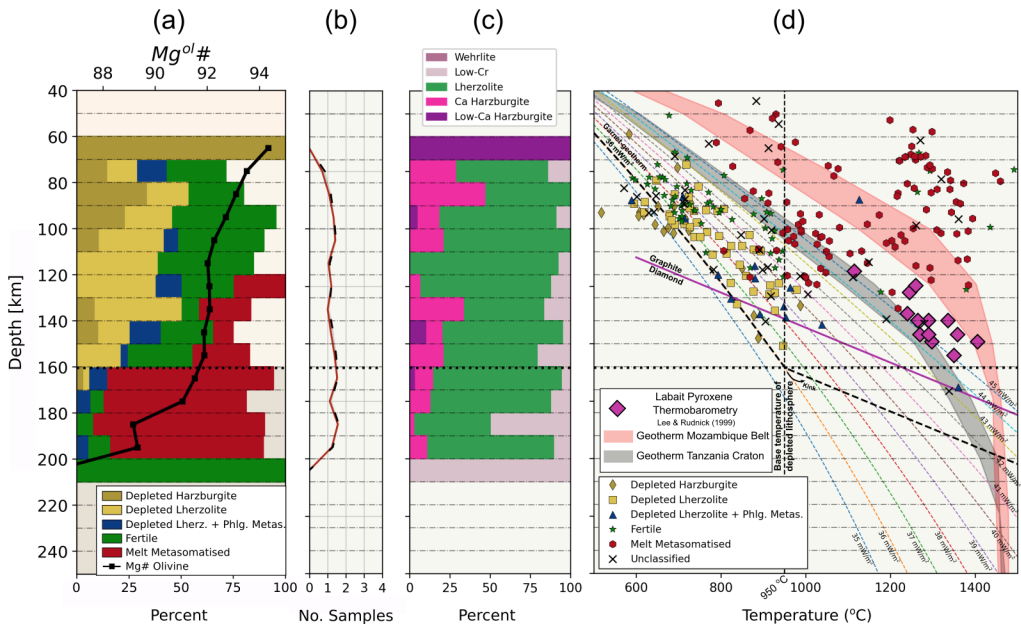
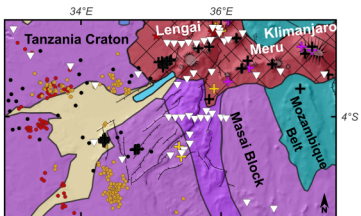
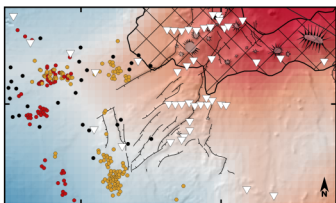


Figure 5.

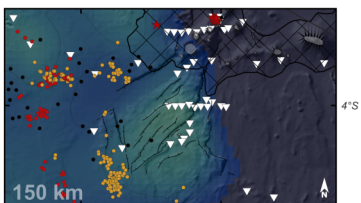
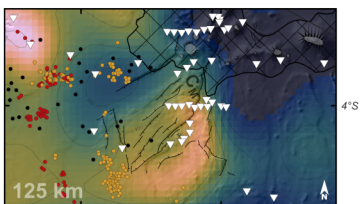
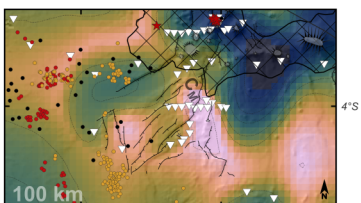
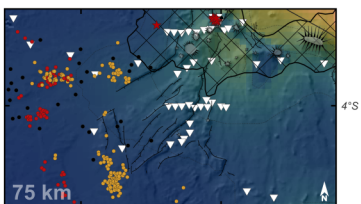
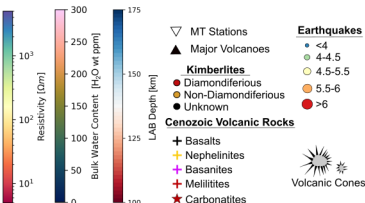
# Geological Map



# LAB Depth



# Water Content Slices



0 50 100 km

# Resistivity Slices

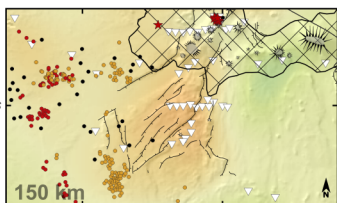
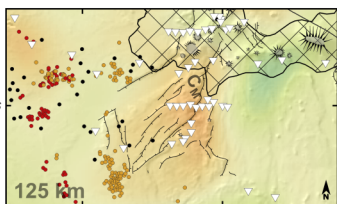
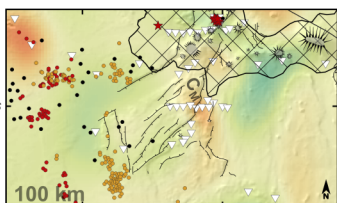
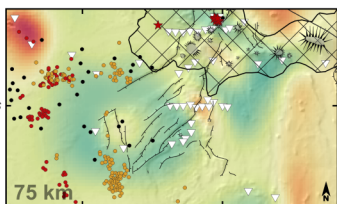
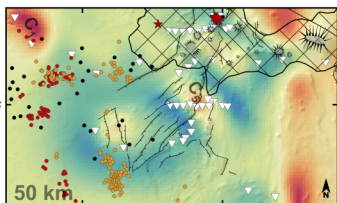
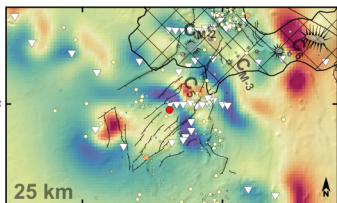
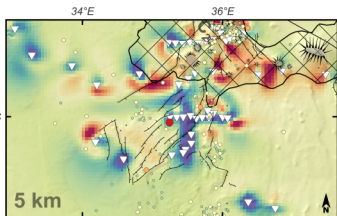




Figure 6.

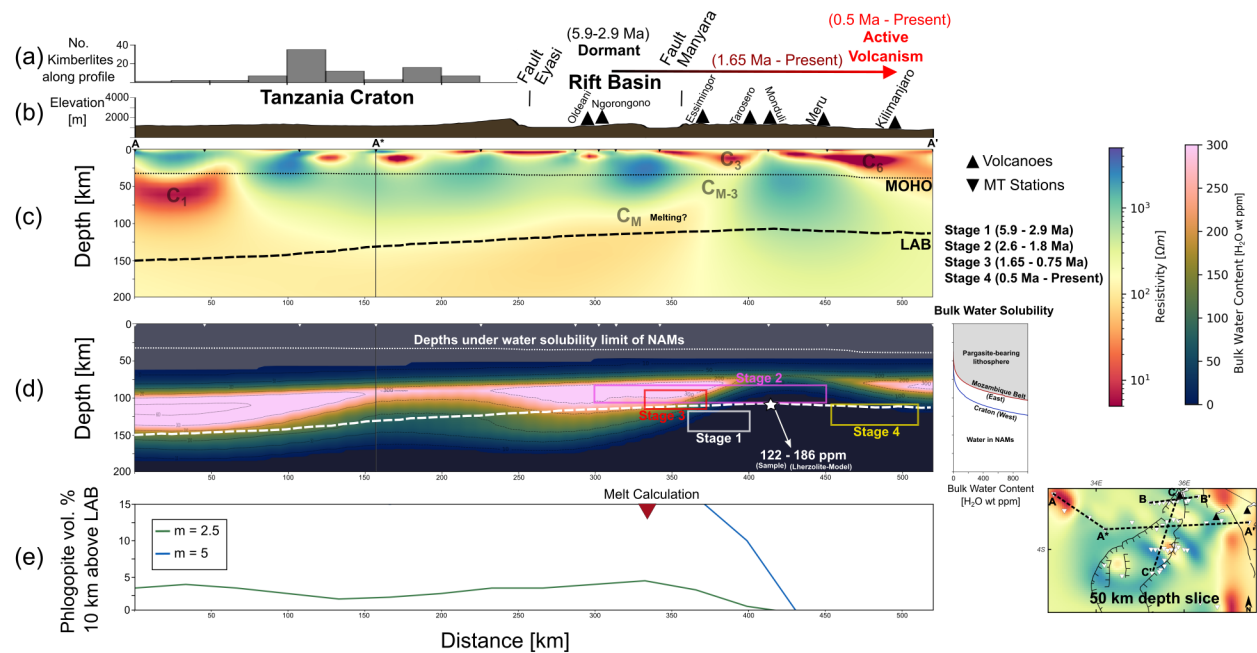


Figure 7.

(2.6 Ma - Present)

**Active  
Volcanism**

(5.9-0.75 Ma)

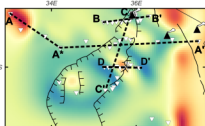
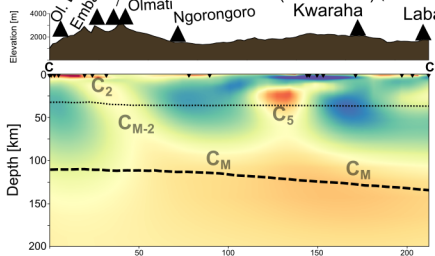
**Dormant**

(1.5-0.9 Ma)

Hanang &

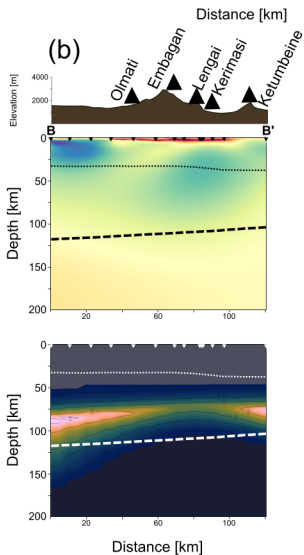
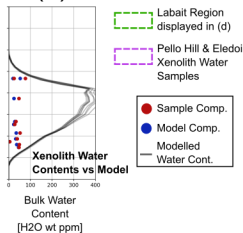
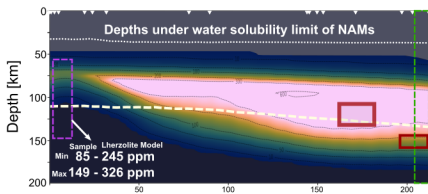
(1.5-0.7 Ma) (0.4-0.2 Ma)

(a)

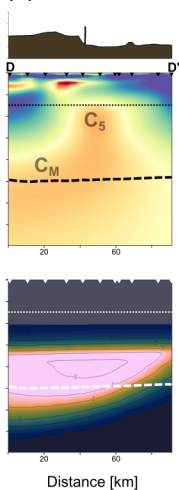


Melted regions from geochemical modelling for Kwaraha and Labait lavas (Baudouin & Parat, 2020).

(d)



(c)



MOHO

LAB

▲ Volcanoes  
▼ MT Stations

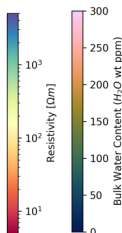


Figure 8.



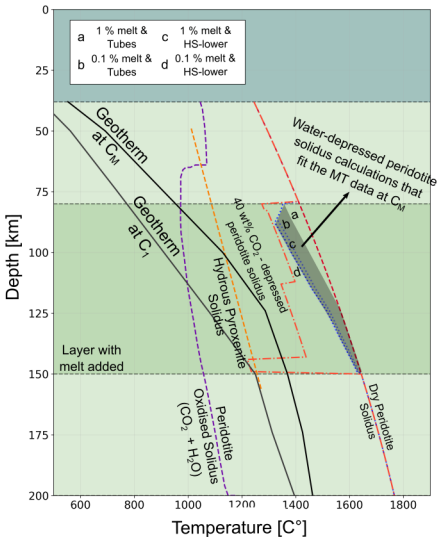


Figure 9.

